

Fassaite composition trends during crystallization of Allende Type B refractory inclusion melts

STEVEN B. SIMON,¹ LAWRENCE GROSSMAN,^{1,2} and ANDREW M. DAVIS²

¹Department of the Geophysical Sciences, The University of Chicago, 5734 South Ellis Avenue, Chicago, IL 60637, USA

²Enrico Fermi Institute, The University of Chicago, 5640 South Ellis Avenue, Chicago, IL 60637, USA

(Received September 25, 1990; accepted in revised form June 20, 1991)

Abstract—Fassaite is a major phase in Type B refractory inclusions and its wide compositional variability makes it an excellent recorder of crystallization-induced changes in liquid composition. Traverses across zoned crystals with electron and ion microprobes show that Ti, V, Sc, Zr and Hf decrease from core to rim, while Mg, Si, REEs, and other trace elements increase. Fassaite/liquid distribution coefficients derived from the compositions of early fassaite and calculated parent liquid compositions are higher than previously reported fassaite D_s , e.g., 0.2–0.8 vs. 0.08–0.5 for the trivalent REEs, possibly due to the high Ti and Al contents of the fassaite we analyzed. Log-log plots of concentrations of elements vs. those of Sc give linear relationships with slopes of $(\bar{D}_i^{xl/L} - 1)/(\bar{D}_{Sc}^{xl/L} - 1)$, where $\bar{D}_i^{xl/L}$ is the bulk crystal/liquid distribution coefficient for element i . From this relationship, we derive effective fassaite/liquid D_s of 2.8 for Sc, 1.5 for Hf, 1.1 for Zr, 0.52 for Y, 0.34 for Ta, 0.29 for Nb, and 0.31–0.48 for trivalent REEs. The effective D_s are applicable to fassaite crystallizing from melts having the compositions and thermal histories of Allende Type B refractory inclusions, and incorporate any equilibrium and kinetic effects that modify D_s during the course of crystallization. Observed fassaite REE contents can be reproduced by a fractional crystallization model in which the effective D_s are used. Ti^{3+} is more compatible in fassaite than Ti^{4+} and, without equilibration of the residual liquid with an external reducing gas, Ti^{3+}/Ti^{tot} ratios (where $Ti^{tot} = Ti^{3+} + Ti^{4+}$) should decrease from core to rim in fassaite crystals. Comparison of profiles of Ti^{3+}/Ti^{tot} ratios in several crystals with those calculated for fractional crystallization suggests that the trend in one crystal was controlled by fractional crystallization alone, but in two others the virtually constant Ti^{3+}/Ti^{tot} ratios may imply that the liquids in these inclusions were able to maintain equilibrium with the solar nebular gas throughout crystallization. Attempts to determine the f_{O_2} of fassaite crystallization on the basis of Ti^{3+}/Ti^{tot} ratios must be based on fassaite grains which are not zoned with respect to Ti^{3+}/Ti^{tot} . The range of observed REE abundances in subliquidus fassaite ($7\text{--}800 \times C1$ for La and $30\text{--}2000 \times C1$ for Lu) now encompasses those in grains previously identified as relict, removing a major reason for their identification as such. Rounded fassaite grains with fairly sharp Mg-rich rims and Ti-rich cores, poikilitically enclosed in mantle melilite in TS34 are candidates for relict grains. The grains are so Sc-rich that they would require extreme prior crystallization of spinel and melilite, which is inconsistent with their very low REE contents (e.g., La at $3\text{--}7 \times C1$). We suggest that the cores of these grains are relict and were trapped *with liquid* during formation of the mantle.

INTRODUCTION

TYPE B, CALCIUM-, aluminum-rich inclusions (CAIs) in carbonaceous chondrites are of great interest because their immediate precursors were phases that are predicted to have formed as early, high-temperature condensates in the solar nebula (GROSSMAN, 1972). GROSSMAN (1975) defined two major types of coarse-grained CAIs: Type A inclusions, which have >75 vol% melilite, plus spinel, hibonite, perovskite, and pyroxene; and Type B inclusions, which contain 25–60% clinopyroxene—the Ti-, Al-rich variety commonly known as fassaite—plus 5–50% melilite, 15–30% Mg-, Al-spinel, and 5–25% anorthite. WARK and LOVERING (1977) further subdivided Type Bs into B1s, which have melilite mantles, and B2s, which do not. Although originally thought to be pristine condensates, Type B inclusions are now believed to have formed from melts of preexisting solids (STOLPER and PAQUE, 1986).

Fassaite is a very important phase in Type B inclusions for several reasons. It is the most abundant phase in B2s and the second most abundant in B1s, after melilite (BECKETT, 1986). Of all the phases in these objects, fassaite is the most variable in major element content. Whereas meteoritic mel-

ilite is essentially a binary solid solution between åkermanite (Åk ; $\text{Ca}_2\text{MgSi}_2\text{O}_7$) and gehlenite ($\text{Ca}_2\text{Al}_2\text{SiO}_7$), fassaite can be well described as a quaternary solid solution of the components Di ($\text{CaMgSi}_2\text{O}_6$), CaTs ($\text{CaAl}_2\text{SiO}_6$), T_3P ($\text{CaTi}^{3+}\text{AlSiO}_6$), and T_4P ($\text{CaTi}^{4+}\text{Al}_2\text{O}_6$) (BECKETT, 1986). The crystal/liquid distribution coefficient of element i in mineral xl , $D_i^{xl/L}$, is defined as the ratio of the concentration of i in solid phase xl to that in a coexisting liquid, L . Another reason for the importance of fassaite is that, with the exception of the high D_s for Eu^{2+} and Sr in all melilite (KUEHNER et al., 1989b) and anorthite and for the rare earth elements (REEs) in aluminous ($<\text{Åk}_{25}$) melilite (KUEHNER et al., 1989b; BECKETT et al., 1990), fassaite has the highest D_s for the large ion lithophile (LIL) elements of all major phases in Type B inclusions. Previous work has shown that, except for La and Ce, fassaite has D_s for the trivalent REEs that are >0.2 (MCKAY et al., 1988). These major and trace element features make fassaite a potentially powerful recorder of crystallization-induced changes in liquid composition. If the bulk composition and crystallization sequence of an inclusion are known, along with the relative proportions and D_s of the crystallizing phases, the amount of prior fractionation needed to attain a given fassaite composition can be estimated. With

this information and sufficient analyses of fassaite in an inclusion, the crystallization history of the inclusion can be reconstructed in some detail.

Fassaite is also important because, as the major Ti-bearing phase in Type B inclusions, its $\text{Ti}^{3+}/\text{Ti}^{4+}$ ratio is used as an indicator of oxygen fugacity (BECKETT and GROSSMAN, 1986). Because fassaite has a higher D for Ti^{3+} than for Ti^{4+} (BECKETT, 1986), it had the ability to concentrate Ti^{3+} into the solid and deplete the residual liquid in Ti^{3+} relative to Ti^{4+} . Therefore, the $\text{Ti}^{3+}/\text{Ti}^{4+}$ ratio of fassaite would have decreased with continued crystallization if the speed of the redox reaction, which otherwise controlled this ratio in the liquid, was insufficient to keep up with the crystallization rate. In this case, an oxygen fugacity determination based on a single fassaite analysis could be incorrect; thus an understanding of the chemical effects of fassaite crystallization is necessary for proper interpretation of $\text{Ti}^{3+}/\text{Ti}^{4+}$ ratios.

Although most fassaite crystals in CAIs are strongly zoned, little systematic work has been done to define and interpret the zoning trends. MACPHERSON and GROSSMAN (1981) noted that Ti and Al decrease from core to rim in fassaite from Allende Type B inclusion TS33, and STOLPER and PAQUE (1986), on the basis of compositions of residual liquids produced in experiments conducted in air, predicted that Ti and Mg would decrease from core to rim. EL GORESY et al. (1985) showed that Ti and Al decrease and Mg increases from core to rim in a concentrically zoned fassaite crystal in Allende Type B1 inclusion USNM 5241. Also, in that same inclusion, REE abundances in fassaite increase from core to rim (MACPHERSON et al., 1989), consistent with concentration into the residual liquid due to incompatible ($D_i^{\text{all}} < 1$) behavior. In spite of the fact that important information such as D s and the path of composition variation of the residual liquid can be learned from zoning trends of fassaite in CAIs, the latter have remained largely uninvestigated because most studies of CAIs have been concerned with other aspects of their petrology. Those studies generally give little or no zoning information and report several "representative" analyses and the range of compositions, omitting locations of analyses within the crystals and not including important components such as Ti^{3+} , Sc, and V in the analyses.

In this paper, we use electron and ion microprobe data to define major, minor, and trace element zoning trends in fassaite from Types B1 and B2 inclusions from the Allende meteorite. We also present calculated fassaite/liquid distribution coefficients for many of the lithophile elements, and discuss evidence for and against the presence of relict fassaite in these inclusions. A preliminary description of this work was given in SIMON and GROSSMAN (1990), SIMON et al. (1990) and DAVIS et al. (1990).

ANALYTICAL METHODS

Scanning Electron Microscopy and Electron Probe Microanalysis

Polished thin sections of Allende CAIs were studied with a petrographic microscope and a JEOL JSM-35 scanning electron microscope (SEM), equipped with a Kevex 7077 energy dispersive X-ray microanalysis system. Mineral compositions were determined with a fully automated Cameca SX-50 electron microprobe, equipped with four wavelength dispersive spectrometers for quantitative analysis and a Kevex energy dispersive X-ray detector, which we used for phase identification. Synthetic glass and crystal (rutile, thortveitite)

and natural mineral (Amelia albite) standards were used. For each analysis, data for major elements were collected at 15 kV with a beam current of 25 nA, and for minor elements (e.g., Sc and V) at 25 kV and 200 nA, using an automated, two-condition program in which beam conditions are stored. In this routine, each point is analyzed for major elements, then the accelerating voltage and beam current are adjusted and the same point is analyzed for minor elements without moving the stage. With counting times of 30 s for Fe and V and 60 s for Sc, detection limits are ≤ 0.005 wt%, based on counting statistics. Background count rates were measured at offsets below and above each peak position for a total counting time equal to that used for the peak. Analysis points were recorded on backscattered electron images (BEIs) of the samples for later relocation in the ion probe. Data were reduced via the modified ZAF correction procedure PAP (POUCHOU and PICHOR, 1984). The analyses gave Ca contents that are very close to one Ca^{2+} ion per six oxygen ions. We therefore assumed that the MgTs ($\text{MgAl}_2\text{SiO}_6$) component is negligible in the fassaite we analyzed. The method of BECKETT (1986) was used for calculating the $\text{Ti}^{3+}/\text{Ti}^{4+}$ ratio necessary to yield four total cations, including exactly one Ca^{2+} ion in the M2 site, per six oxygen ions. For analyses with less than ~ 4 wt% $\text{TiO}_2^{\text{tot}}$ (all Ti calculated as TiO_2), amounts of Ti^{3+} and Ti^{4+} so calculated are not accurate because the error on Ti^{3+} depends on the cumulative analytical uncertainties in the concentrations of many other elements. For Ti^{3+} , the 1σ uncertainty due to this effect is typically ~ 0.01 cations per 6 oxygens, regardless of the amount of Ti^{3+} present.

Ion Microprobe Analysis

Major, minor, and trace element analyses were collected with a modified AEI IM-20 ion microprobe, using a mass-filtered 20 kV $^{16}\text{O}^+$ primary beam, on spots previously analyzed by electron microprobe. The primary beam current of 10–25 nA produced a beam spot 15–30 μm in diameter. Techniques are outlined in HINTON et al. (1988) and DAVIS et al. (1991). All data were collected using energy-filtering to suppress molecular interferences. Ca-normalized ion yields and relative MO^+/M^+ ratios for REEs and Y were determined from synthetic glasses (DRAKE and WEILL, 1972). Ion yields for Nb, Hf, Ta, Th, and U were determined from NBS 611 glass; for V, Cr, and Sr from synthetic glasses prepared by Corning; for Sc, Zr, and Ba from a synthetic Åk_{60} glass prepared at Caltech; and for Na, Mg, Al, Si, and Ti from a variety of glasses and minerals used as electron microprobe standards. Previous experience has shown that the ion yield for Si relative to Ca ranges from 0.38 to 0.52 among common silicate minerals for the energy filtering conditions used on the University of Chicago ion microprobe. For this reason, the ion yield for Si was adjusted for each analysis such that the SiO_2 contents obtained by ion and electron microprobe agreed. Ion yields for all other elements measured are much less sensitive to matrix effects, so the same ion yields were used for all silicate minerals. Each spot was analyzed by "burning in" with the primary ion beam for two minutes, then collecting data at each mass peak sequentially. For each spot, six cycles through the mass spectrum were made over a period of about one hour. The count rates were plotted vs. the cycle number to ensure that the beam remained on a single phase without passing into other phases or through tiny inclusions. Major element analyses agree with electron microprobe values within $\pm 10\%$ (relative) for clean fassaite, but are not shown because the electron microprobe analyses are more accurate. When analyzing some of the smaller relict fassaite grains, the beam overlapped onto adjacent melilite or spinel. For these spots, the fassaite composition was determined by calculating the proportions of phases in the analysis from major elements and subtracting the melilite contribution to the trace element content based on analysis of adjacent, clean melilite.

PETROGRAPHY AND PETROLOGY OF TYPE B INCLUSIONS

Petrographic Descriptions of the Inclusions

TS22

TS22 is a Type B2 inclusion first described by GROSSMAN (1975). It has coarse (~ 1 mm), concentrically zoned fassaite

grains, melilite crystals up to 3 mm long, and minor anorthite, all poikilitically enclosing numerous $\sim 10\text{--}20\ \mu\text{m}$ spinel crystals. The fassaite crystals are anhedral to nearly euhedral and are so choked with spinel that spinel-free areas large enough for ion probe analysis are rare. For this reason, ion probe analyses were not performed on fassaite in this sample. Modal proportions of the phases, as determined by BECKETT (1986), are 26% spinel, 26.5% fassaite, 24% melilite, 18% alteration products and 5.5% anorthite. Alteration products in this and the inclusions described below typically consist of grossular, monticellite, wollastonite, aluminous diopside, nepheline and sodalite. In general, melilite is the only phase in Type B inclusions that underwent any significant alteration (MACPHERSON et al., 1981; BARBER et al., 1984). Trace element data for this inclusion were reported by GROSSMAN and GANAPATHY (1976) and GROSSMAN et al. (1977).

TS23

This is a large Type B1 inclusion with a melilite-rich mantle and a fassaite-rich interior. Melilite crystals are lathlike and up to 1.5 mm long. Fassaite is present as blocky, anhedral to subhedral crystals and as small anhedral grains and rims on spinel, both of which are poikilitically enclosed in melilite, as described by KUEHNER et al. (1989a). Some of the large fassaite grains enclose numerous spinel crystals, some are spinel-free, and others have both spinel-rich and spinel-free zones. BECKETT (1986) determined that $\sim 45\%$ of this inclusion consists of the melilite mantle, which contains 4% fassaite and $\sim 3\%$ spinel, the remainder being 66% melilite and 27% alteration products. His mode for the interior of TS23 is 32.4% melilite, 30.9% fassaite, 15.0% spinel, 5.1% anorthite, 0.4% perovskite, and 16.1% alteration products. This inclusion has also been studied by GROSSMAN (1975), MACPHERSON et al. (1984), and MURRELL and BURNETT (1987).

TS33

This inclusion was thoroughly described by MACPHERSON and GROSSMAN (1981) who cited petrographic and mineral chemical evidence that it crystallized from a liquid. Although it is considered a Type B1 inclusion by some workers (BECKETT, 1986; MACPHERSON, pers. comm., 1990), it appears to be intermediate between B1s and B2s, having characteristics common to both types. It has melilite crystals at its rim that project radially inward (MACPHERSON and GROSSMAN, 1981) but they do not form an easily distinguished, nearly monomineralic mantle. The inclusion consists of melilite laths up to 5 mm long, with interstitial fassaite and anorthite, all poikilitically enclosing spinel. Fassaite is more abundant in the interior of the inclusion than at the rim, where it occurs as anhedral crystals, $\sim 0.4\text{--}1$ mm across, between melilite crystals. At the rim, melilite is more abundant than fassaite and both are finer-grained than in the core (MACPHERSON and GROSSMAN, 1981). Because of the lack of a clear boundary between them, BECKETT (1986) did not perform separate core-mantle modes for TS33, as he did for other B1 inclusions. His mode for this inclusion is 42.9% melilite, 31.0% fassaite, 10.6% spinel, 4.7% anorthite, and 10.8% alteration products.

TS34

This inclusion is a cm-sized Type B1 CAI. The melilite mantle is ~ 1.5 mm wide and contains only 3% fassaite and 4% spinel, which occur as poikilitic inclusions. The interior of the inclusion is dominated by blocky, anhedral to subhedral fassaite crystals, most of which are optically zoned and poikilitically enclose spinel crystals. One large, zoned melilite crystal protrudes from the inner edge of the mantle into the fassaite-rich interior of the inclusion. A plane-light photomicrograph of the entire inclusion (identified as A13S4) is shown in Fig. 4 of CLAYTON et al. (1977). The mode of the interior of the inclusion, given by BECKETT (1986), is 46.3% fassaite, 32.0% melilite, 14.3% spinel, 1.7% anorthite, and 5.7% alteration products.

Crystallization Sequences of Type B Inclusions

Much of the interpretation of petrographic observations and chemical data presented here is done from the perspective of the experimentally determined liquid-crystal phase relations in one bulk composition representative of Type B inclusions (STOLPER, 1982; STOLPER and PAQUE, 1986). The order of appearance of phases in equilibrium crystallization, with the possible exception of rare, melilite-rich Type B1 or very pyroxene-rich Type B2 compositions (J. BECKETT, pers. comm., 1990), is spinel first, followed by melilite, anorthite and fassaite. MACPHERSON et al. (1984) found, however, that anorthite nucleation could be suppressed relative to fassaite at cooling rates between 0.5 and 50°C/hr . In this case, melilite is followed directly by fassaite. The incoming of fassaite in the absence of anorthite increases the Al/Mg ratio of the residual liquid because the fassaite has a lower Al/Mg ratio than that liquid. This causes an increase in the Al/Mg ratio of the cocrystallizing melilite, which has the effect of reversing the outward zoning of individual crystals from normal (decreasing in Al/Mg ratio) to reverse (increasing in Al/Mg ratio). The onset of anorthite crystallization later depletes the residual liquid in Al, allowing the melilite to return to normal zoning (MACPHERSON et al., 1984). Melilite crystals with normally zoned cores and reversely zoned rims occur in TS23 and TS34.

Whether anorthite crystallization is suppressed or not, fassaite is preceded by spinel and spinel + melilite crystallization over a range of about 300°C (STOLPER, 1982; STOLPER and PAQUE, 1986). Because spinel and melilite have very low D_s for the LIL elements, except for Eu^{2+} and Sr in melilite (KUEHNER et al., 1989b), crystallization of spinel and melilite drives up the concentrations of the other REEs and incompatible elements in the residual liquid. Thus, fassaite crystallizes from a liquid which is relatively enriched in LIL elements compared to the starting liquid. As will be shown later, fassaite has somewhat higher D_s than spinel and melilite for many trace elements, making it an excellent recorder of changes in liquid composition.

Occurrence of Fassaite in the Inclusions

In this paper, we distinguish four textural types of fassaite: large, blocky crystals; irregularly shaped grains poikilitically enclosed in melilite in the interiors of inclusions; rounded

grains poikilitically enclosed in the melilite mantle of TS34; and both intergranular and poikilitic fassaite in the melilite mantle of TS23.

The large, blocky fassaite crystals, also referred to as sub-liquidus, clearly crystallized from the same liquid as the rest of the inclusion as part of the normal crystallization sequence. They occur in the cores of Type B1 inclusions and throughout B2s. Such grains may poikilitically enclose many small spinel crystals, as in TS22; or in a given inclusion, some crystals or parts thereof may be spinel-rich and others may be spinel-free, probably depending on when and where they formed and how quickly they grew. For example, early slow growth may result in exclusion of preexisting spinel crystals.

The second type of fassaite, observed in TS23, TS33, and TS34, occurs as rims on spinel and between spinel grains enclosed in melilite, as described by MACPHERSON *et al.* (1984) and, in TS23, by KUEHNER *et al.* (1989a). The rims are generally $\sim 10\ \mu\text{m}$ wide. This type of fassaite also occurs as curved, meniscus-like fillings between spinel grains (Fig. 1a), as irregularly shaped grains enclosing spinel crystals (Fig. 1b), and as small ($<30\ \mu\text{m}$), anhedral, spinel-free crystals, all poikilitically enclosed in melilite, Åk_{30-40} . In BEIs (Fig. 1), in which albedo correlates with mean atomic number, some of the larger grains are seen to have light and dark zones separated by straight, sharp boundaries. It can be inferred that the light regions are higher in Ti than the dark regions. Many of the fassaite grains enclosed in melilite have very thin ($\sim 1\ \mu\text{m}$) rims in contact with melilite. Examples are shown in Fig. 2. The rims are too thin to analyze by electron probe but can be seen in BEIs as a uniform light band adjacent to fassaite and a dark band between the light rim and the host melilite. This textural relationship of fassaite inside gehlenitic melilite is expected neither from the equilibrium crystallization sequence nor from experimental data (MACPHERSON *et al.*, 1984), which predict that melilite compositions approach Åk_{65} before fassaite nucleates. Therefore, fassaite should not be found in melilite crystals that are more aluminous than Åk_{65} . This has led to the suggestion that such fassaite grains are relict and predate formation of the parent liquid of the inclusion (KUEHNER *et al.*, 1989a).

A third fassaite type occurs in the mantle of TS34, where it is present as rounded, zoned grains up to $70\ \mu\text{m}$ across, poikilitically enclosed in aluminous (Åk_{25-35}) melilite. By contrast, the fourth type of fassaite, that in the melilite mantle of TS23, occurs as intergranular crystals up to 1 mm across and as small ($1\text{--}20\ \mu\text{m}$) grains poikilitically enclosed in melilite. Some of the grains in the mantle of TS34 are concentrically zoned, having rims that are uniform in thickness (up to about $3\ \mu\text{m}$) and that follow the edges of the fassaite grains (Fig. 3b). Others are asymmetrically zoned with thicker, low-Z rims on one side than on the opposite side (Fig. 3a). Electron microprobe analysis shows that the rims have lower TiO_2 and higher MgO contents (by about 1–3 wt%) than the cores, which are richer in Ti than fassaite elsewhere in the inclusion. Rims such as these are not observed in fassaite that is poikilitically enclosed in melilite in the interior of the inclusion, nor in fassaite that occurs in the mantle of TS23. Thin rims like those on interior poikilitic fassaite in TS34 (Fig. 2) are not observed around mantle fassaite in TS34, and the latter is not associated with spinel.

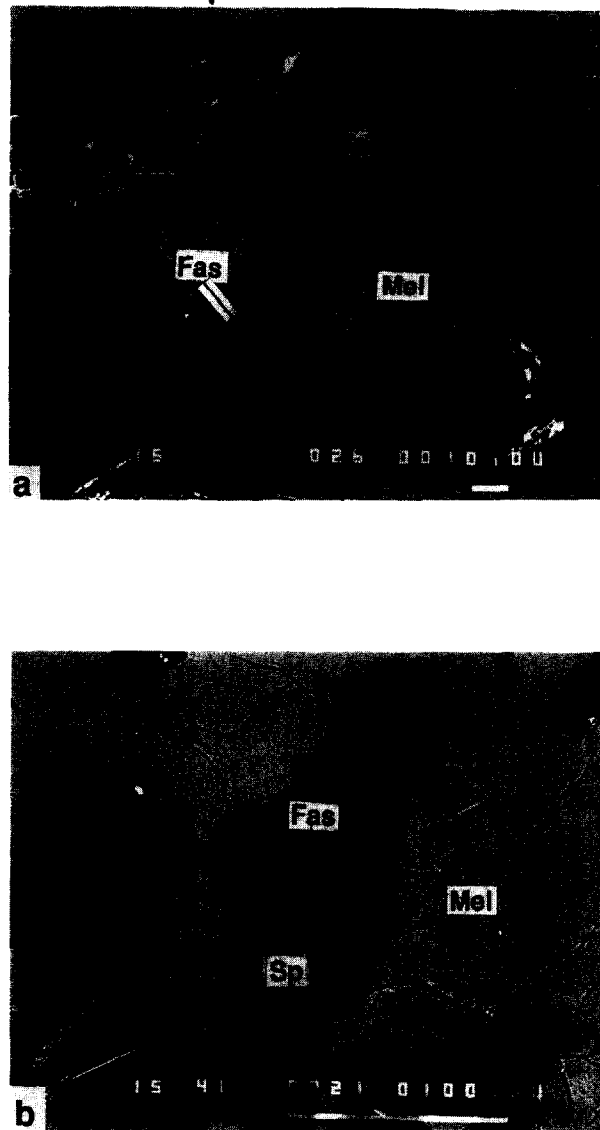


FIG. 1. Backscattered electron images (BEIs) of fassaite (Fas) poikilitically enclosed in interior melilite (Mel) in TS34. (a) Meniscus-like fassaite linking spinel crystals (Sp). Scale bar is $10\ \mu\text{m}$. (b) Fassaite linking and enclosing spinel crystals. Note light and dark zones in the large fassaite crystal, and anhedral fassaite adjacent to spinel at left and lower right. Scale bar is $100\ \mu\text{m}$.

Another difference between the mantle fassaite in TS34 and the poikilitic grains in the interior of the inclusion is that the mantle grains are rounded on all sides, as shown in Fig. 3, whereas the interior grains have rounded corners but may have straight sides (Fig. 1b). Yet another difference, which can be seen by comparison of Fig. 1 with Fig. 3, is the light and dark zones in the interior poikilitic grains, which are not observed in the mantle grains. From textural criteria, the mantle is probably the first part of B1s to crystallize (MACPHERSON and GROSSMAN, 1981), as it contains the highest-temperature, most aluminous melilite, e.g., Åk_{1-35} in TS34. The occurrence of fassaite grains in the mantle is not easily understood, as fassaite is not predicted to form until the melilite reaches $\sim \text{Åk}_{65}$ in composition.

A feature associated with the poikilitic fassaite grains, both in the interior of inclusions and in the mantles of TS34 and

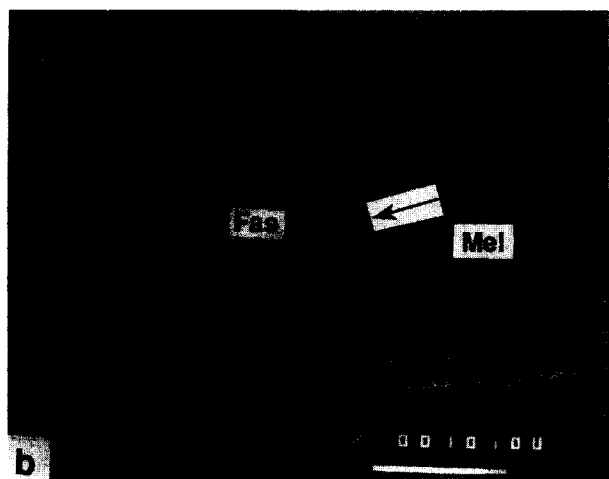


FIG. 2. The rims (indicated by arrows) on poikilitic fassaite in interior melilite in TS34. Scale bars are 10 μm . BEI.

TS23, is the $\text{\AA}k$ enrichment that occurs in the melilite immediately adjacent to many of the fassaite grains. We have observed enrichments from the “background” levels ($\sim \text{\AA}k_{30}$) up to $\text{\AA}k_{54}$, with most “enriched” analyses in the $\text{\AA}k_{40-50}$ range. The enrichment zones do not appear to be continuous rims around the grains, like those described by MACPHERSON et al. (1989) around fassaite in the mantle of USNM 5241. Based on our analyses, in most cases in the mantle as well as in the interior, melilite adjacent to fassaite may have “normal” composition on one side of the fassaite grain and be $\text{\AA}k$ -enriched on the other. Normal and enriched compositions can also occur on the same side of a fassaite grain. Enrichment zones do not extend too far from the edges of fassaite grains—generally less than 10 μm .

FASSAITE CRYSTAL CHEMISTRY

A brief review of pyroxene crystal chemistry will help us understand the wide range of fassaite compositions. The gen-

eral pyroxene formula is XYZ_2O_6 , where X and Y are octahedrally coordinated divalent cations in the M2 and M1 sites respectively, and Z is tetrahedrally coordinated Si^{4+} . Where X is a large cation, such as Ca, the site becomes somewhat distorted and is eight-coordinated. Substitution of trivalent (e.g., Ti^{3+} , Sc^{3+} , REE^{3+}) or tetravalent (e.g., Ti^{4+} , Zr^{4+}) cations in either M1 or M2 creates a charge excess which is balanced by a coupled substitution of Al^{3+} for Si^{4+} in the tetrahedral site. Fassaite in CAIs probably represents the extreme case of such substitution in pyroxene.

As shown by DOWTY and CLARK (1973), Allende fassaite is a $C2/c$ clinopyroxene with a structure similar to that of diopside. The tetrahedral site is filled by Si and Al; DOWTY and CLARK (1973) found no evidence for any other cations in this site. The largest cation site, M2, is filled by Ca (DOWTY and CLARK, 1973; BECKETT, 1986) and is therefore

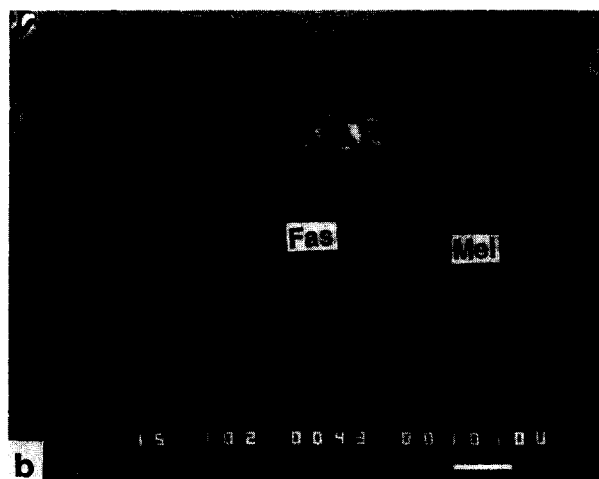
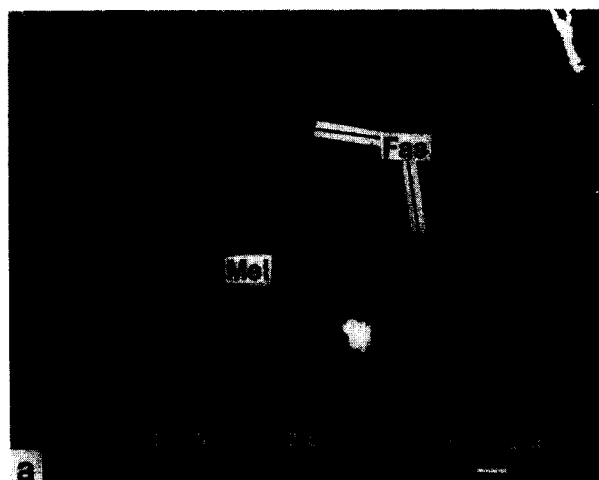


FIG. 3. Fassaite enclosed in the melilite mantle of TS34. Scale bars are 10 μm . BEIs. (a) Note dark rim in small fassaite grain, and the brightness of the large grain compared to the host melilite. Contrast with darkness of fassaite relative to melilite in Figs. 1 and 2. (b) Fassaite with relatively thick, sharp rim.

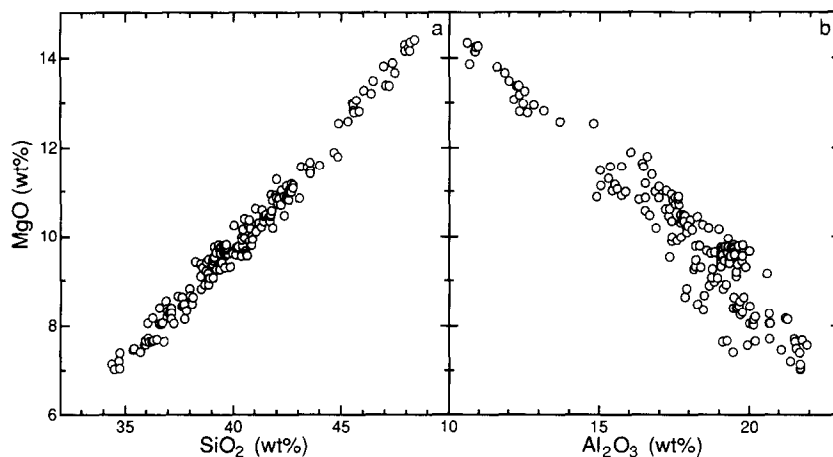


FIG. 4. MgO, SiO₂ and Al₂O₃ abundances in subliquidus fassaite in TS22, TS23, TS33 and TS34. (a) MgO vs. SiO₂. (b) MgO vs. Al₂O₃.

8-coordinated. Pyroxene/liquid *Ds* for REEs generally increase with increasing Ca in pyroxene (MCKAY et al., 1986). This is probably because Ca has the effect of enlarging the M2 site (PAPIKE et al., 1988; SHEARER et al., 1989), which makes it easier for the REEs to enter the structure. In contrast, an orthopyroxene which has its M2 sites predominantly filled by Mg will have much smaller M2 sites than a Ca-rich clinopyroxene (CAMERON and PAPIKE, 1981) and will have much lower *Ds* for the REEs (PAPIKE et al., 1988), as will pigeonite (MCKAY et al., 1986, 1990; SHEARER et al., 1989).

The M1 site in fassaite is smaller than the M2 and is 6-coordinated. In Allende fassaite, the M1 site is mainly occupied by Mg, Ti³⁺, Ti⁴⁺, and Al, plus minor amounts of Sc, V, Fe²⁺, and Cr³⁺. Much of the variability in major and minor element abundances in fassaite is achieved by entry of various divalent, trivalent, and tetravalent cations into the M1 site, coupled with appropriate Si-Al substitution in the tetrahedral site to maintain charge balance. Divalent cations, of course, do not require substitution of Al for Si to maintain charge balance and Mg is by far the dominant divalent cation that enters the M1 site in Allende fassaite. As a result, MgO and SiO₂ contents of subliquidus fassaite are strongly correlated (Fig. 4a), and MgO and Al₂O₃ are strongly anticorrelated (Fig. 4b). HAZEN and FINGER (1977) observed similar relationships in fassaite from the Angra dos Reis meteorite. The complete correlation matrix for major and minor elements in 120 electron probe analyses of 12 subliquidus fassaite crystals in four inclusions is given in Table 1. Calculations using a nonparametric technique (the Spearman correlation) give similar results. For this many analyses, even a correlation

coefficient of 0.25 is significant at the 99% confidence level. In addition to the strong correlation between MgO and SiO₂ ($r = 0.98$), the results show that Sc₂O₃, Ti₂O₃, and TiO₂ are positively correlated with Al₂O₃, as would be expected from the coupled substitutions required for charge balance. Note also the positive correlations between Sc₂O₃ and Ti₂O₃, V₂O₃ and Ti₂O₃, and V₂O₃ and Sc₂O₃, indicating similar geochemical behavior. The strong anticorrelation between MgO and Al₂O₃ ($r = -0.86$) and the filling of the M2 site by Ca (DOWTY and CLARK, 1973) indicate that the MgTs component is negligible.

FASSAITE COMPOSITIONS IN TYPE B INCLUSIONS

Major and Minor Elements

In addition to the crystal chemical constraints discussed earlier in this paper, the other major factors that affect fassaite compositions in these inclusions include the composition of the parent liquid, crystal growth rates, the relative amounts of other phases present, and their *Ds*. To determine how fassaite composition changes as crystallization proceeds, we performed electron probe traverses across five concentrically zoned, blocky crystals of fassaite, i.e., the first type of fassaite described earlier in this paper. Some of the results are shown in Fig. 5 and, for different traverses, Table 2. In the latter, the innermost point of the traverse across one of the grains in TS34 did not pass through the core and is therefore labelled "interior" (Table 2, col. 6). In Fig. 5 we plotted oxide abundance against distance from the core of each of three crystals. The crystals display similar systematics and it is clear that

Table 1. Correlation coefficients for major and minor elements in fassaite based on 120 electron microprobe analyses

	MgO	Al ₂ O ₃	SiO ₂	CaO	TiO ₂	Ti ₂ O ₃	V ₂ O ₃	FeO	Sc ₂ O ₃
MgO	1.000								
Al ₂ O ₃	-0.864	1.000							
SiO ₂	0.980	-0.864	1.000						
CaO	0.646	-0.444	0.648	1.000					
TiO ₂	-0.525	0.614	-0.617	-0.268	1.000				
Ti ₂ O ₃	-0.787	0.385	-0.722	-0.587	0.151	1.000			
V ₂ O ₃	-0.303	0.062	-0.267	0.003	0.103	0.529	1.000		
FeO	0.033	0.046	0.008	0.073	0.140	-0.139	-0.099	1.000	
Sc ₂ O ₃	-0.695	0.351	-0.686	-0.492	0.356	0.848	0.450	-0.083	1.000

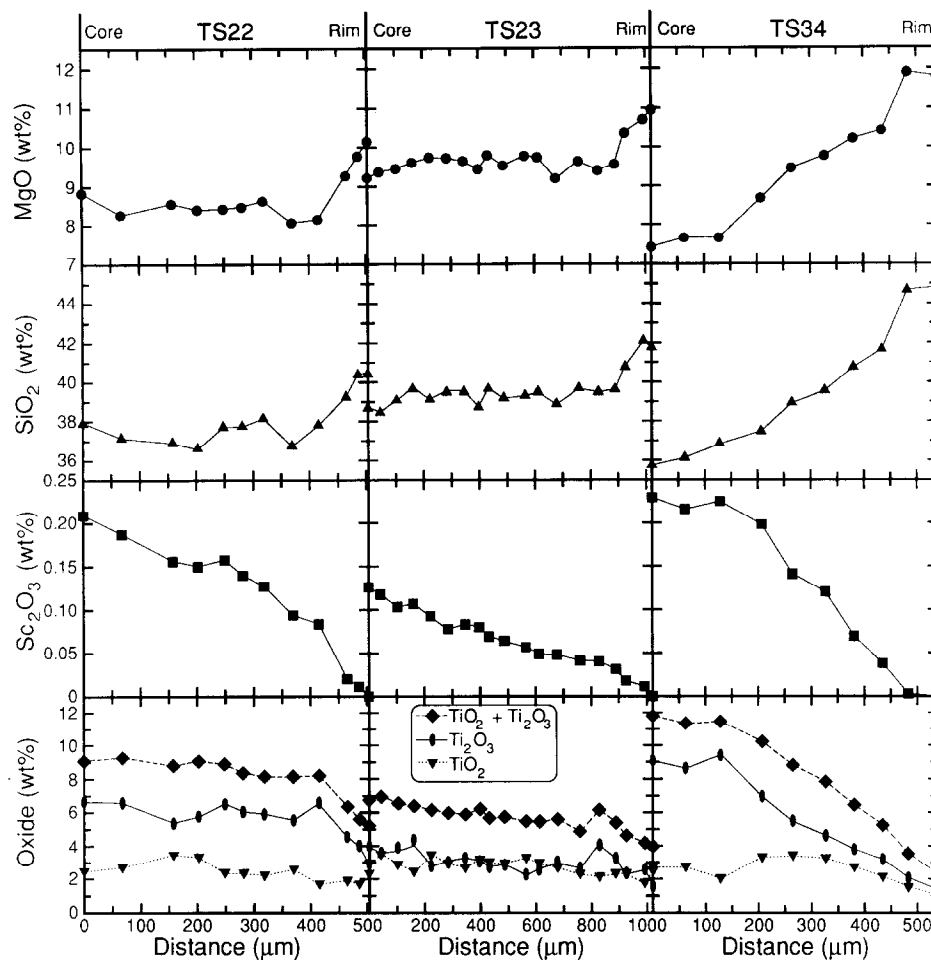


FIG. 5. Results of electron microprobe traverses across large, blocky, zoned fassaite crystals in TS22 (left), TS23 (center) and TS34 (right). Data for a given oxide are plotted at the same vertical scale for all inclusions to simplify comparisons, and are shown as a function of distance from the core of the crystal. Note the general similarity of the zoning trends in fassaite from each inclusion.

early fassaite (core) tends to be Sc- and Ti-rich and Mg- and Si-poor relative to late fassaite (crystal rims). The close Sc-Ti^{3+} and Mg-Si correlations are obvious from these plots.

The crystal from TS34 (Fig. 5) exhibits monotonic increases in MgO and SiO_2 from core to rim, whereas the crystals in TS22 and TS33 have relatively homogeneous interiors and sharply zoned rims with respect to these elements. Not all crystals are symmetrically zoned. Some crystals grew preferentially in one direction relative to the others, probably reflecting limitations imposed by adjacent crystals and/or local variations in liquid composition caused by, for example, isolation of melt pockets that could have occurred as crystallization reached completion.

The zoning trends (Fig. 5) show that Sc contents decrease from core to rim. Strong partitioning of Sc into fassaite depletes the residual liquid, causing Sc contents in the fassaite (Table 2) to decrease as crystallization proceeds. Before fassaite begins to crystallize, the incompatibility of Sc in spinel (NAGASAWA *et al.*, 1980) and melilite (BECKETT *et al.*, 1990) allows crystallization of these phases to drive up the Sc content of the residual liquid from the bulk level of ~ 100 ppm (GROSSMAN *et al.*, 1977) so that fassaite begins crystallizing with >0.2 wt% Sc_2O_3 .

Profiles of V_2O_3 are like those of Sc_2O_3 in that V_2O_3 contents decrease progressively from core to rim in fassaite (Table 2). We noticed a variation, from inclusion to inclusion, of over a factor of three in the $\text{V}_2\text{O}_3/\text{Sc}_2\text{O}_3$ ratio of the earliest fassaite. Although it is certain that this ratio can be affected by differences in bulk $\text{V}_2\text{O}_3/\text{Sc}_2\text{O}_3$ ratios, it is equally clear that it is also strongly influenced by variations from inclusion to inclusion in the absolute and relative amounts of spinel and melilite that crystallized prior to fassaite. In the inclusions studied here, melilite contains <30 ppm V_2O_3 and <15 ppm Sc_2O_3 , suggesting that both elements are incompatible in melilite. Spinel contains 0.2–0.6 wt% V_2O_3 and virtually no Sc_2O_3 , suggesting that V_2O_3 is compatible and Sc_2O_3 incompatible in spinel. Crystallization of spinel and melilite from a Type B CAI melt should therefore change the $\text{V}_2\text{O}_3/\text{Sc}_2\text{O}_3$ ratio of the residual liquid and the fassaite that later crystallizes from it. Perhaps this is why the earliest TS22 fassaite, poikilitically enclosing copious spinel crystals, has a $\text{V}_2\text{O}_3/\text{Sc}_2\text{O}_3$ ratio of 0.7, while that in TS34, with only \sim one-third as much prior spinel, has a $\text{V}_2\text{O}_3/\text{Sc}_2\text{O}_3$ ratio of 2.4.

Titanium is compatible in fassaite and decreases in abundance from core to rim (Fig. 5). The Ti^{3+} cation has a larger radius than the Ti^{4+} cation (SHANNON and PREWITT, 1969),

Table 2. Compositions of fassaite determined by electron probe (oxides) and ion microprobe (trace elements).

	CORE	TS34				RIM	INTERIOR	TS34		RIM	CORE	TS33		RIM
	1.	2.	3.	4.	5.	6.	7.	8.	9.	10.	11.	12.		
MgO	7.89	8.98	10.99	10.51	12.87	9.63	11.76	11.54	11.88	7.67	8.16	10.17		
Al ₂ O ₃	18.98	18.05	15.63	18.87	14.66	16.87	15.81	16.72	16.53	21.77	21.27	19.00		
SiO ₂	37.37	38.84	42.43	42.28	45.92	39.82	43.89	43.70	43.64	35.99	37.13	40.77		
CaO	24.63	24.98	25.16	25.36	25.67	25.00	25.44	25.64	24.98	24.31	24.54	24.78		
TiO ₂ ^{tot}	12.17	10.36	6.78	4.67	2.46*	9.39	4.47	3.46*	2.91*	9.73	8.58	4.60		
V ₂ O ₃	0.54	0.47	0.18	0.20	0.04	0.43	0.04	0.06	0.04	0.21	0.17	0.04		
FeO	BLD	0.01	0.01	0.01	0.30	0.01	0.03	0.02	0.02	BLD	BLD	BLD		
Sc ₂ O ₃	0.22	0.18	0.08	BLD	BLD	0.17	0.02	BLD	BLD	0.17	0.13	0.01		
Ti ₂ O ₃	9.08	7.08	4.30	2.56	0.19	6.32	2.21	1.58	0.49	5.86	5.20	2.12		
TiO ₂	1.94	2.41	1.95	1.77	2.22	2.30	1.97	1.69	2.32	3.07	2.69	2.18		
TOTAL	100.65	101.00	100.72	101.53	101.87	100.55	101.17	100.95	99.90	99.05	99.29	99.07		
Si	1.380	1.424	1.542	1.513	1.630	1.464	1.577	1.574	1.576	1.338	1.374	1.495		
IVAl	0.620	0.576	0.458	0.487	0.370	0.536	0.423	0.426	0.424	0.662	0.626	0.505		
Tet. Sum	2.000	2.000	2.000	2.000	2.000	2.000	2.000	2.000	2.000	2.000	2.000	2.000		
VIAl	0.206	0.204	0.211	0.309	0.243	0.195	0.246	0.284	0.280	0.292	0.302	0.316		
Mg	0.434	0.491	0.596	0.561	0.681	0.528	0.630	0.620	0.640	0.425	0.450	0.556		
Ca	1.000	1.000	1.000	1.000	1.000	1.000	1.000	1.000	1.000	1.000	1.000	1.000		
V	0.015	0.013	0.005	0.005	0.001	0.012	0.001	0.002	0.001	0.006	0.005	0.001		
Fe	0	0	0	0	0.009	0	0.001	0.001	0.001	0	0	0		
Sc	0.007	0.006	0.002	0	0	0.005	0.001	0	0	0.005	0.004	0		
Ti ³⁺	0.283	0.219	0.132	0.077	0.006	0.196	0.067	0.048	0.015	0.185	0.163	0.066		
Ti ⁴⁺	0.054	0.067	0.054	0.048	0.060	0.064	0.054	0.046	0.064	0.087	0.076	0.061		
Oct. Sum	2.000	2.000	2.000	2.000	2.000	2.000	2.000	2.001	2.001	2.000	2.000	2.000		
Ti ³⁺ /Ti ^{tot}	0.840	0.766	0.710	0.616	0.091	0.754	0.554	0.511	0.190	0.680	0.682	0.520		
TRACE ELEMENTS (ppm)														
La	2.64	2.36	3.65	13.70	2.71	4.36	7.53	10.44	2.25	2.53	7.48			
Ce	10.8	8.56	12.9	41.9	10.6	16.4	27.9	39.6	8.40	9.60	29.7			
Pr	2.00 ± 0.21	2.47 ± 0.24	2.48 ± 0.25	6.99 ± 0.42	2.65 ± 0.25	3.42 ± 0.29	4.19 ± 0.31	7.26 ± 0.38	1.62 ± 0.17	1.69 ± 0.19	5.41 ± 0.33			
Nd	11.5 ± 0.8	11.5 ± 0.9	15.2 ± 1.0	34.1	10.9 ± 0.8	17.3 ± 1.1	25.8	40.3	8.85 ± 0.63	11.5 ± 0.8	28.6			
Sm	5.37 ± 0.31	5.06 ± 0.32	6.44 ± 0.37	11.59	5.55	8.44	10.4	16.7	4.9	4.41 ± 0.28	11.9			
Eu	0.25 ± 0.03	0.26 ± 0.03	0.35 ± 0.04	0.45 ± 0.05	0.25 ± 0.03	0.51 ± 0.05	0.58 ± 0.05	0.64 ± 0.05	0.29 ± 0.03	0.33 ± 0.03	0.62 ± 0.05			
Gd	7.57 ± 0.55	6.86 ± 0.61	9.55 ± 0.66	17.3 ± 1.0	6.87 ± 0.57	13.15 ± 0.73	16.75	28.1	7.33 ± 0.47	7.20 ± 0.52	19.89			
Tb	1.53 ± 0.13	1.50 ± 0.14	2.03 ± 0.16	3.24 ± 0.21	1.63 ± 0.14	2.59 ± 0.18	3.37 ± 0.20	5.27	1.29 ± 0.11	1.25 ± 0.12	3.89 ± 0.20			
Dy	9.34	10.13 ± 0.51	12.30	23.47	9.71	17.01	21.54	35.8	9.51	10.5	27.2			
Ho	1.90 ± 0.17	1.94 ± 0.18	2.66 ± 0.21	5.31 ± 0.30	1.96 ± 0.17	3.57 ± 0.24	4.06 ± 0.25	7.32	1.96 ± 0.15	2.74 ± 0.19	6.29			
Er	6.07	6.83	7.90	15.88	6.12	11.33	14.26	23.7	6.08	7.55	19.24			
Tm	1.15 ± 0.08	1.06 ± 0.08	1.46 ± 0.10	2.73 ± 0.14	1.21 ± 0.09	1.82 ± 0.11	2.28 ± 0.12	4.06	0.79 ± 0.06	1.09 ± 0.08	2.93			
Yb	5.71 ± 0.38	5.27 ± 0.39	7.18 ± 0.46	12.37	6.36 ± 0.41	10.7 ± 0.5	12.0 ± 0.6	19.2	5.52 ± 0.33	6.73 ± 0.39	16.2			
Lu	1.31 ± 0.10	0.99 ± 0.10	1.27 ± 0.11	2.37 ± 0.15	1.16 ± 0.10	1.99 ± 0.13	2.09 ± 0.14	3.86	1.07 ± 0.08	1.33 ± 0.10	3.32			
Na	9.2 ± 0.6	12.34 ± 0.70	43.59	51.56	8.7 ± 0.6	16.3	9.2 ± 0.6	7.1 ± 0.5	211	39.1	43.1			
Sc	1451	1307	586	124	1102	198	110	73.0	1236	873	100			
Cr	158 ± 11	219 ± 13	411	235 ± 14	257 ± 14	531	351	489	209 ± 11	245 ± 13	377			
V	3020	2536	838	1590	2295	150 ± 9	691	173	1304	755	103			
Sr	27.7 ± 5.7	< 12.6	38.2 ± 5.7	< 15.4	40.4 ± 5.3	39.6 ± 5.9	37.2 ± 7.0	< 13.2	39.5	32.5	41.6			
Y	55.0	55.2	67.8	123	63.1	93.4	115	181	58.5	68.0	181			
Zr	429	360	346	272	410	354	292	401	368	390	447			
Nb	2.26 ± 0.31	2.52 ± 0.35	2.29 ± 0.34	8.54 ± 0.66	3.37 ± 0.39	2.33 ± 0.33	5.21 ± 0.49	6.97 ± 0.52	2.86 ± 0.31	2.42 ± 0.31	5.21 ± 0.46			
Ba	0.18 ± 0.10	0.37 ± 0.14	3.16 ± 0.41	8.44 ± 0.68	0.35 ± 0.14	0.55 ± 0.18	6.94 ± 0.59	0.18 ± 0.12	1.47 ± 0.23	0.13 ± 0.09	0.15 ± 0.11			
Hf	16.29	12.79 ± 0.51	9.17	4.81 ± 0.44	12.78	6.60 ± 0.42	5.50 ± 0.41	6.24 ± 0.47	10.7	10.8	6.60 ± 0.41			
Ta	0.38 ± 0.15	0.33 ± 0.16	0.20 ± 0.17	0.51 ± 0.24	0.35 ± 0.15	0.25 ± 0.18	1.07 ± 0.22	0.71 ± 0.25	0.66 ± 0.15	< 0.30	1.01 ± 0.22			
Th	0.11 ± 0.04	0.08 ± 0.04	0.37 ± 0.08	2.62 ± 0.20	0.09 ± 0.04	0.27 ± 0.06	0.74 ± 0.10	0.78 ± 0.10	0.11 ± 0.04	0.23 ± 0.06	0.68 ± 0.09			
U	0.03 ± 0.02	0.04 ± 0.03	0.04 ± 0.03	0.35 ± 0.08	0.05 ± 0.03	< 0.05	0.10 ± 0.04	0.17 ± 0.05	0.08 ± 0.03	0.04 ± 0.03	0.15 ± 0.04			

BLD: below limit of detection of electron microprobe.

Errors given are $\pm 1\sigma$, based on counting statistics, and are only given where they exceed 5% of the amount present; upper limits are $< 2\sigma$.* Ti³⁺ and Ti⁴⁺ values are not accurate for analyses with less than ~4 wt% TiO₂^{tot} (Ti as TiO₂) because of the large relative errors associated with small cation abundances.

which gives the former a better fit into the pyroxene M1 site (PAPIKE et al., 1988). This results in a $D_{\text{Ti}^{3+}}^{\text{fas/L}}$ that is higher than $D_{\text{Ti}^{4+}}^{\text{fas/L}}$, as found by BECKETT (1986). If no other factors were involved, the Ti³⁺/Ti⁴⁺ ratio in a fassaite crystal would be expected to decrease from core to rim because fassaite crystallization should deplete the residual liquid in Ti³⁺ relative to Ti⁴⁺. More will be said of this later.

As can be inferred from the anticorrelations of MgO with TiO₂ and Ti₂O₃ in Table 1, as total Ti contents in fassaite decrease, MgO contents increase (Fig. 6). This is accomplished by the exchange reactions, $\text{Ti}^{3+} + \text{IVAl}^{3+} \rightleftharpoons \text{Mg}^{2+} + \text{Si}^{4+}$ and $\text{Ti}^{4+} + 2 \text{IVAl}^{3+} \rightleftharpoons \text{Mg}^{2+} + 2 \text{Si}^{4+}$, where IVAl refers to Al in the tetrahedral site. Al also enters pyroxene as Tschermak's molecule via the reaction $\text{IVAl}^{3+} + \text{VIAl}^{3+} \rightleftharpoons \text{Mg}^{2+} + \text{Si}^{4+}$. When Al₂O₃ is plotted against TiO₂ + Ti₂O₃ (Fig. 7a), a gen-

erally positive trend with some scatter (probably due to the CaTs component) is seen: up to about 22 wt% Al₂O₃ and 8 wt% Ti oxides. Higher Ti contents occur but without further increases in Al₂O₃, although Ti must substitute with Al to maintain charge balance, as shown by the previously mentioned reactions. This apparent contradiction is resolved by plotting the same analyses in terms of their IVAl and VIAl (octahedral Al) contents against Ti³⁺ + Ti⁴⁺ (Fig. 7b). This plot shows that IVAl increases with Ti but, at high Ti contents, VIAl decreases, causing the bulk Al content to stay about the same. The decrease in VIAl at high Ti contents may simply be due to increased cationic competition for the site.

Analyses of fassaite grains from the mantle of TS34 have been plotted in Figs. 6 and 7 with different symbols to distinguish them from subliquidus fassaite. Representative

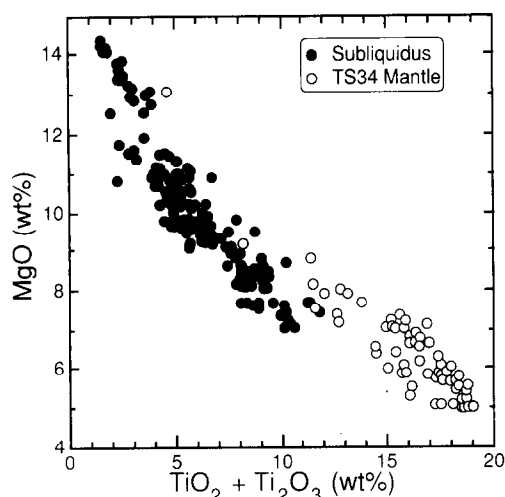


FIG. 6. Plot of MgO vs. total Ti oxides in fassaite in all four inclusions in this study, including fassaite in the mantle of TS34. Analyses of rims of mantle fassaite overlap with those of subliquidus fassaite, but analyses of mantle fassaite cores do not.

analyses of two different grains are given in Table 3 and labelled "mantle fassaite." The latter fassaite has the highest Ti and Sc contents and the lowest REE contents of all of our analyses of fassaite from this inclusion. These are features expected for the earliest fassaite to crystallize, because Ti and Sc are compatible in fassaite and the REEs are incompatible, as indicated by the zoning trends revealed along traverses across five single crystals (Fig. 5 and Table 2). Because of their very high Ti contents, TS34 mantle fassaite grains have very high ^{IV}Al proportions. As shown in Fig. 7b, they extend the Al-Ti trends defined by subliquidus fassaite to higher ^{IV}Al and lower ^{VI}Al contents. Note the slight overlap between mantle and subliquidus fassaite compositions in both the ^{IV}Al -Ti and ^{VI}Al -Ti trends. The TS34 mantle fassaite grains are greatly enriched in Ti relative to subliquidus grains, with 16–20 wt% TiO_2^{tot} in the former and up to 12 wt% TiO_2^{tot} in the latter, but the mantle grains commonly have rims (Fig. 3) which are lower in Ti (9–14 wt% TiO_2^{tot}) than their cores and whose compositions are within the observed range for subliquidus fassaite.

The TS34 mantle grains also contrast sharply with subliquidus fassaite in terms of their Sc contents, which are very high (Table 3). Sc_2O_3 contents in mantle fassaite cores range from 0.2 to 1.2 wt%, with most between 0.4 and 0.9 (rims have from 0 to 0.4 wt%), whereas the maximum Sc_2O_3 content in our analyses of subliquidus fassaite is about 0.25 wt%.

Trace Elements

We determined the trace element contents of fassaite in three inclusions with the ion microprobe. Representative data are given in Tables 2 and 3. Note that Sc and V abundances were determined by both electron probe and ion probe. Data from the two probes agree rather well in the analyses of the large zoned grains (Table 2), but not so well for the TS34 mantle grains (Table 3, analyses 1 and 2). The reasons for lack of agreement in the latter analyses are the relatively strong

zoning of the grains, the different beam diameters ($\sim 4 \mu m$ in the electron probe and 20–30 μm in the ion probe) of the instruments, and the different sample volumes analyzed by the instruments. Sc_2O_3 in fassaite crystals in the mantle of TS34 typically varies from ~ 0.9 wt% at the core to <0.2 wt% at the rim over a distance of less than 25 μm . In analysis of these grains, therefore, the electron probe can analyze pure core (high- Sc_2O_3) fassaite, whereas the ion probe will likely sample core and rim (low- Sc_2O_3) fassaite simultaneously.

Chondrite-normalized REE and Y abundances in all fassaite analyzed in TS23, TS33, and TS34 are shown in Fig. 8. Most analyses have a positive slope from La through Sm, a large negative Eu anomaly, and relatively flat heavy REE (HREE) abundances at levels slightly higher than those of the light REEs (LREEs) and with small negative Yb anomalies. The low La and Ce abundances are not surprising because the clinopyroxene/liquid D_s for these elements are the lowest (MCKAY et al., 1988) and the melilite/liquid D_s are the highest (KUEHNER et al., 1989b; BECKETT et al., 1990) of all the REEs. The negative Eu anomalies also probably reflect prior fractionation by melilite (MASON and MARTIN, 1974). The negative Yb anomalies may be caused by bulk Yb depletions. Crystal/liquid fractionation is unlikely to create a negative Yb anomaly because even solar nebular oxygen

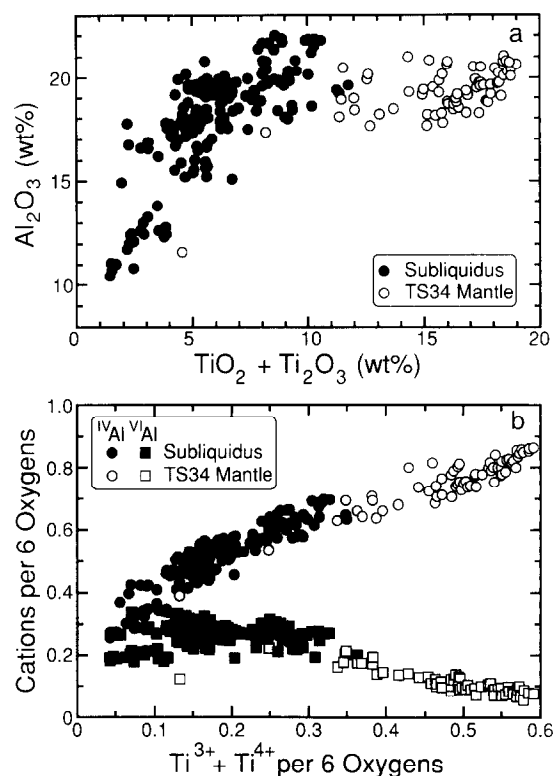


FIG. 7. Al-Ti relationships in fassaite in all four inclusions in this study, including fassaite in the mantle of TS34. (a) Al_2O_3 vs. total Ti oxides, showing a general trend of increasing Al_2O_3 with Ti in subliquidus pyroxene, which levels off at the high Ti contents of TS34 mantle fassaite. (b) ^{IV}Al and ^{VI}Al vs. total Ti cations per 6 oxygen ions. With increasing Ti, ^{IV}Al increases as required for charge balance, while ^{VI}Al remains the same in subliquidus fassaite and decreases in TS34 mantle fassaite.

Table 3. Compositions of mantle fassaite in TS34 and late fassaite in TS34 and TS23.

	<-----Mantle fassaite----->		<-----Late fassaite----->			C1	
	1.	2.	3.	4.	5.	6.	Chondrites†
MgO (wt %)	5.08	5.10	10.02	10.57	11.72	13.99	
Al ₂ O ₃	20.34	20.28	20.38	18.20	16.31	11.72	
SiO ₂	30.90	30.46	41.27	42.48	43.49	46.38	
CaO	24.89	25.16	24.91	25.54	25.34	24.42	
TiO ₂ ^{tot}	18.50	19.25	3.70*	4.30*	3.42*	1.50*	
V ₂ O ₃	1.35	0.93	0.07	0.02	0.01	BLD	
FeO	0.01	0.01	0.01	0.01	0.02	0.01	
Sc ₂ O ₃	0.80	0.67	BLD	BLD	BLD	BLD	
Ti ₂ O ₃	13.60	13.96	1.67	2.74	1.16	—	
TiO ₂	3.64	4.15	1.78	1.24	2.10	—	
TOTAL	100.61	100.72	100.11	100.80	100.12	97.96	
Si	1.187	1.175	1.490	1.536	1.576	1.693	
Al	0.813	0.825	0.510	0.464	0.424	0.307	
Tot. Sum	2.000	2.000	2.000	2.000	2.000	2.000	
VI _{Al}	0.108	0.098	0.358	0.312	0.273	0.197	
Mg	0.291	0.293	0.539	0.570	0.633	0.761	
Ca	1.000	1.000	1.000	1.000	1.000	1.000	
V	0.039	0.027	0.002	0.001	0	0	
Fe	0	0	0	0	0.001	0	
Sc	0.027	0.023	0	0	0	0	
Ti ³⁺	0.431	0.441	0.051	0.083	0.035		
Ti ⁴⁺	0.104	0.118	0.049	0.034	0.058		0.041
Oct. Sum	2.000	2.000	1.999	2.000	2.000	1.999	
Ti ³⁺ /Ti tot	0.806	0.789	0.509	0.711	0.381	—	
<i>Trace Elements (ppm)</i>							
La	0.70 ± 0.09	0.82 ± 0.09	64.2	53.7	34.5	194.8	0.235
Ce	3.66 ± 0.33	3.72 ± 0.32	187.1	179.5	117.9	609.6	0.603
Pr	1.08 ± 0.24	1.36 ± 0.26	30.7	30.0	20.0	102.8	0.089
Nd	4.30 ± 0.78	5.56 ± 0.84	130.9	158.4	104.5	516.0	0.452
Sm	3.42 ± 0.30	3.67 ± 0.29	41.7	51.3	38.6	165.9	0.147
Eu	0.38 ± 0.06	0.30 ± 0.05	3.0 ± 0.2	1.2	0.98 ± 0.06	6.9	0.056
Gd	2.06 ± 0.59	3.38 ± 0.62	65.4 ± 3.4	76.9	62.7	256.7	0.197
Tb	0.67 ± 0.14	0.81 ± 0.14	12.9 ± 0.7	14.3	11.7	49.7	0.036
Dy	3.89 ± 0.47	4.73 ± 0.49	86.3 ± 2.6	99.2	77.0	373.3	0.243
Ho	0.89 ± 0.18	1.26 ± 0.20	17.9 ± 0.9	21.0	16.5	91.9	0.056
Er	2.50 ± 0.31	2.92 ± 0.31	58.5	67.9	52.0	317.1	0.159
Tm	0.86 ± 0.11	0.67 ± 0.10	11.5 ± 0.5	11.3	8.6	44.9	0.024
Yb	2.39 ± 0.39	1.94 ± 0.35	53.4 ± 2.2	52.2	40.7	266.8	0.162
Lu	0.48 ± 0.11	1.01 ± 0.13	9.7 ± 0.5	10.7	8.1	49.6	0.024
Na	13.8 ± 1.1	12.5 ± 1.0	195.2	98.1	32.6	7079	5000
Sc	5863	3119	41.9 ± 3.2	29.8	28.4	2.9 ± 0.9	5.82
Cr	32.7 ± 8.4	65.0 ± 8.9	326	695	697	603	2660
V	8769	3532	489	316	45.4 ± 8.1	48.4 ± 8.3	56.5
Sr	22.1 ± 9.8	30.2 ± 9.4	153 ± 19	113 ± 8	40.1 ± 8.6	411	7.80
Y	25.8	29.4	468	577	407	2693	1.56
Zr	1049	1032	477	732	620	1659	3.94
Nb	5.0 ± 0.7	4.2 ± 0.6	117	42.1	33.9	138	0.246
Ba	2.5 ± 0.5	0.6 ± 0.2	111	19.1	12.7 ± 0.8	1714	2.34
Hf	34.7	26.7	4.9 ± 1.3	7.7 ± 0.6	7.8 ± 0.6	13.8 ± 1.2	0.104
Ta	< 0.39	< 0.34	7.9 ± 1.0	5.5 ± 0.4	3.4 ± 0.4	13.6 ± 0.9	0.014
Th	< 0.11	0.07 ± 0.06	12.8 ± 0.8	9.4	6.0	18.3	0.294
U	< 0.09	< 0.05	1.4 ± 0.3	1.3 ± 0.1	0.54 ± 0.09	2.5 ± 0.2	0.008

BLD: below detection limit of electron microprobe.

Errors given are ± 1 σ, based on counting statistics, and are only given where they exceed 5 % of the amount present; upper limits are < 2 σ.

*Ti³⁺ and Ti⁴⁺ values are not accurate for analyses with less than ~ 4 wt % TiO₂^{tot}.[†]Anders and Grevesse (1989)

fugacities are not sufficiently reducing to stabilize a significant fraction of the Yb as Yb²⁺ in condensed phases. The higher volatility of Yb relative to the other HREEs (BOYNTON, 1975; DAVIS and GROSSMAN, 1979) can cause it to be separated during condensation or evaporation.

Trivalent REEs are incompatible elements in CAI phases, preferring to remain in the liquid rather than enter the structures of spinel, fassaite, anorthite, and all melilite more åkermanitic than Åk₆ (KUEHNER et al., 1989b). As crystallization proceeds, REE concentrations in the liquid increase, and fassaite records these changes. If $D_{\text{REE}}^{\text{fas/L}}$ does not decrease with decreasing temperature, fassaite that crystallizes from late, REE-rich liquids should have higher REE contents than that which crystallizes from early, REE-poor liquids. To test these predictions and to determine the full range of trace element abundances in fassaite, we analyzed very early fassaite

to find the lowest abundances and late fassaite to determine the highest. Fassaite that crystallized early is found at the cores of large crystals and in the melilite mantles of Type B1 inclusions, either between or poikilitically enclosed within melilite crystals. As previously mentioned, early fassaite in each inclusion is richer in Ti and Sc than other fassaite in the same inclusion. Fassaite in the mantle of TS34 is even richer in Ti and Sc but the origin of this fassaite is not clear (see Discussion). Late fassaite is found at the rims of large crystals such as those whose compositions are given in Table 2. In inclusions TS23 and TS34, which have melilite crystals with reversely zoned rims, anorthite began crystallizing after fassaite (MACPHERSON et al., 1984), making anorthite the last phase to appear. Therefore, fassaite which appears from its texture to have crystallized with or after anorthite must have formed late. An example is in Fig. 9, in which part of

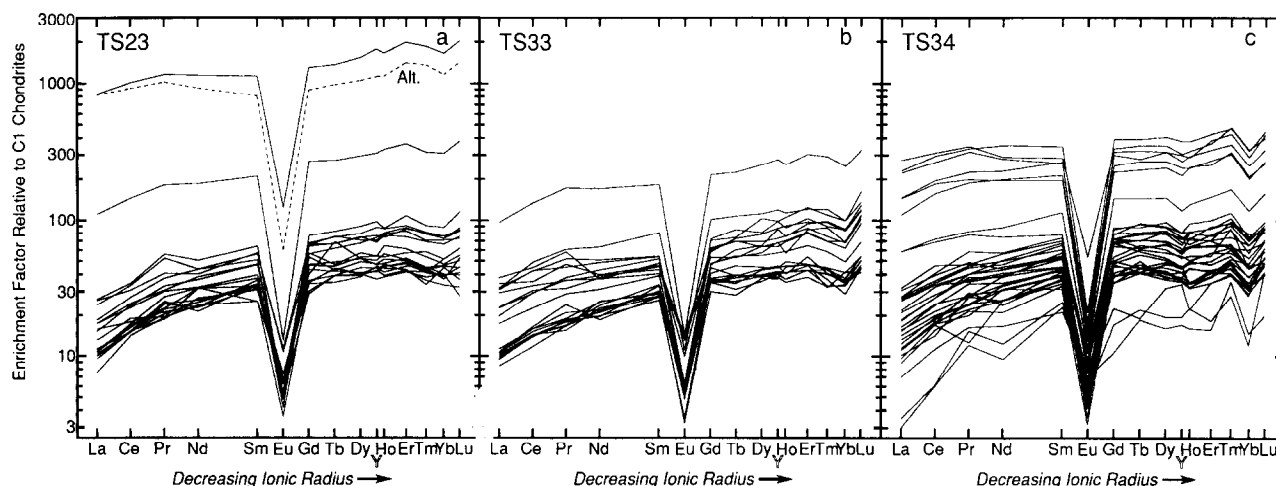


FIG. 8. C1 chondrite-normalized REE and Y abundances in fassaite in TS23, TS33 and TS34, determined by ion microprobe. Dashed line in Fig. 8a is an analysis of a grossular-monticellite-wollastonite assemblage near the late fassaite overgrowth shown in Fig. 9. C1 chondrite normalization values are from ANDERS and GREVESSE (1989).

a fassaite crystal in TS23 has grown around a preexisting anorthite crystal. An analysis of this overgrowth around the anorthite (Table 3, col. 6) along with analyses of three late fassaite crystals from TS34, yielded the highest REE contents ever found in fassaite: $\sim 1000 \times C1$ (LREE) and $\sim 2000 \times C1$ (HREE). Analysis of a $20 \mu\text{m}$ spot in the adjacent assemblage of grossular, monticellite, and wollastonite ("Alt" in Figs. 8a and 9) shows that it also has very high REE contents and an enrichment pattern (dashed line in Fig. 8a) very similar to that of the fassaite overgrowth. This suggests that the fassaite and the precursor of these alteration products crystallized from the same, extremely fractionated liquid. Of the fassaite analyzed for this study, that with the lowest REE contents ($3\text{--}30 \times C1$) is found in the mantle of TS34. Representative analyses of this fassaite are also given in Table 3, cols. 1 and 2.

To summarize: REE abundances in fassaite in TS34 range from $3\text{--}300 \times C1$ for La and $20\text{--}310 \times C1$ for Lu; in TS33, $10\text{--}100 \times C1$ for La and $45\text{--}325 \times C1$ for Lu; and in TS23, $7\text{--}800 \times C1$ for La and $30\text{--}2000 \times C1$ for Lu.

Abundances of other LIL trace elements (Ta, Nb, Th, U) in fassaite vary as expected: very low in early crystals, higher in late crystals (Tables 2 and 3). As is the case for most REEs, the observed range of compositions is about one order of magnitude. As seen below, two trace elements, Zr and Hf, are compatible in fassaite. This is the reason Hf, like Ti and Sc, decrease in abundance from core to rim in all of the profiles in Table 2. Zr is much less compatible than Hf in fassaite, as will be seen later, and its concentration falls from core to rim in two of the profiles in Table 2 and rises in the other.

When plotted against Sc concentrations on log-log plots (Fig. 10), the concentrations of most of these elements define linear trends which reflect the fact that their effective D_s relative to that of Sc are essentially constant throughout most of the interval of fassaite crystallization (discussed later). For the blocky, subliquidus fassaite, the only major deviations from the trends are at low values of Sc, which correspond to very late-stage crystallization.

DISCUSSION

Fassaite/Liquid Distribution Coefficients

Equilibrium crystal/melt distribution coefficients have not been measured for pyroxene of the composition found in Type B CAIs. Our trace element data on fassaite in several Type B inclusions can be used in two ways to infer distribution coefficients. First, the composition of the liquid when fassaite began to crystallize is calculated from the inclusion's bulk composition and the amount of prior crystallization of melilite and spinel. The composition of this liquid is compared with that of early-crystallized fassaite to obtain distribution coefficients. In the second method, distribution coefficients are obtained from the slopes of log trace element vs. log Sc plots.

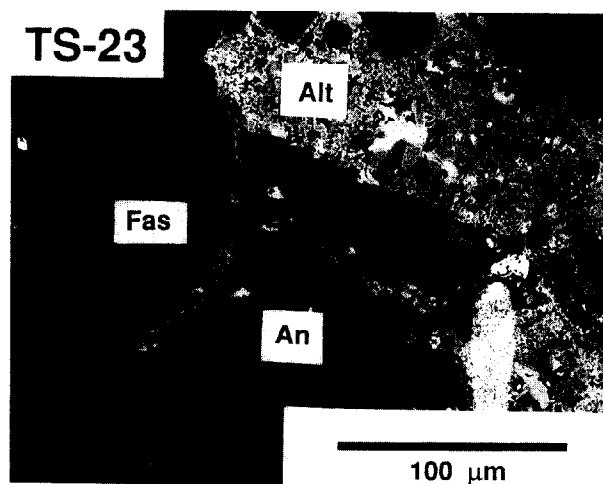


FIG. 9. BEI of a location in TS23 where fassaite (Fas) has grown around a crystal of anorthite (An). Because anorthite was the last phase to begin crystallizing in this inclusion, the fassaite overgrowth must have formed from a late-stage, highly fractionated liquid. The end of the overgrowth appears lighter because of its enrichment in REEs and other large-ion lithophiles. Alt represents alteration products; the chondrite-normalized REE pattern for this material is shown in Fig. 8a.

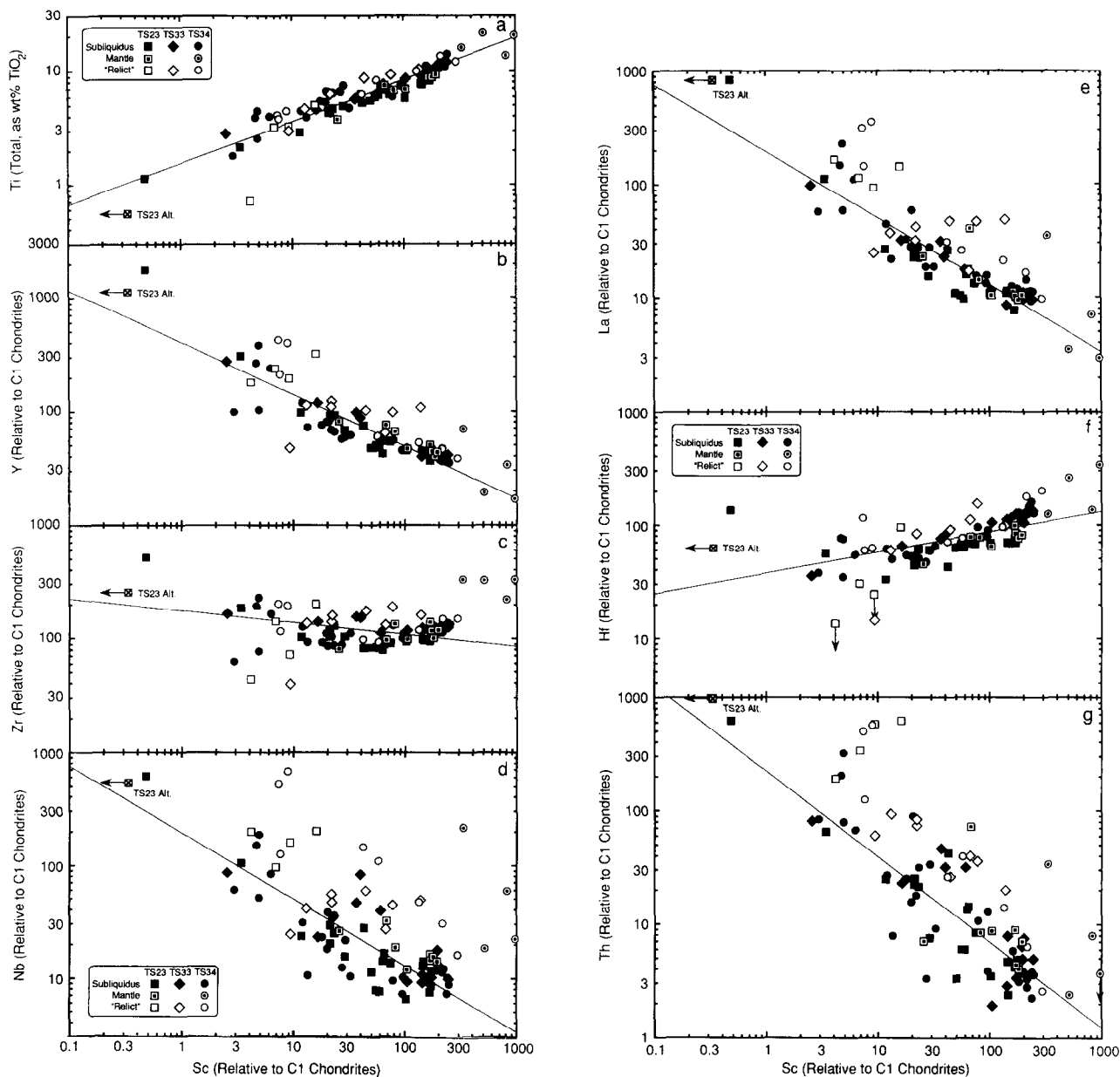


FIG. 10. Log-log plots of wt% $\text{TiO}_2^{\text{tot}}$ and C1 chondrite-normalized abundances of selected trace elements vs. C1 chondrite-normalized Sc abundances in fassaite. Regression lines were calculated from all subliquidus points. A strongly compatible element (Ti) gives a positive slope; an incompatible element (La) gives a negative slope and a weakly compatible element (Zr) gives a slightly negative slope. Error bars are shown where they are larger than the symbol. The point labelled TS23 Alt. is the grossular-monticellite-wollastonite assemblage near the late fassaite overgrowth shown in Fig. 9.

First Method

Using this method, we calculated $D_{\text{Sc}}^{\text{fas/L}}$ for TS23, TS33, and TS34. For each inclusion, three quantities are required: the bulk Sc content, the amount of crystallization prior to the appearance of fassaite, and the Sc content of the first fassaite to crystallize.

As the bulk Sc contents of these inclusions have not been measured, we assumed that they have the average C1 chondrite-normalized refractory lithophile element enrichment factor of Allende coarse-grained inclusions, 18.6 (GROSSMAN

et al., 1977). This corresponds to a Sc concentration of 113 ppm.

Modal proportions of phases in the three CAIs were determined by point-counting of thin sections by BECKETT (1986). To obtain the fraction of fassaite crystallizing in the assemblage that crystallizes after the first appearance of fassaite, we assumed that the proportions of phases crystallizing at the eutectic in the system Ge-Fo-An-Sp (STOLPER, 1982) are identical to those that crystallized throughout the interval of fassaite solidification in the inclusions, even though the CAIs we studied have significant TiO_2 contents and melilite

Table 4. Fassaite/liquid distribution coefficients in Type B CAI's. Uncertainties in means are standard errors of measurements of the three individual CAI's.

	$D_{Sc}^{fas/L}$, for early fassaite				Slope of $\log t$ vs. $\log Sc$				Effective $D_{Sc}^{fas/L}$
	TS23	TS33	TS34	Mean	TS23	TS33	TS34	Mean	
Sc	2.19	4.60	3.82	3.54 ± 0.71					2.84 ± 0.39
Y	0.65	0.97	0.71	0.78 ± 0.10	-0.45	-0.46	-0.47	-0.46 ± 0.01	0.52 ± 0.01
Zr	1.36	2.64	2.15	2.05 ± 0.37	-0.17	-0.08	-0.07	-0.11 ± 0.03	1.08 ± 0.04
Nb	0.15	0.29	0.17	0.20 ± 0.04	-0.63	-0.43	-0.73	-0.60 ± 0.09	0.29 ± 0.11
La	0.17	0.26	0.22	0.22 ± 0.03	-0.56	-0.53	-0.68	-0.59 ± 0.04	0.31 ± 0.06
Ce	0.27	0.38	0.34	0.33 ± 0.03	-0.52	-0.53	-0.63	-0.56 ± 0.04	0.36 ± 0.04
Pr	0.38	0.49	0.47	0.45 ± 0.03	-0.60	-0.52	-0.64	-0.59 ± 0.03	0.31 ± 0.04
Nd	0.48	0.54	0.55	0.52 ± 0.02	-0.52	-0.48	-0.60	-0.53 ± 0.04	0.39 ± 0.05
Sm	0.52	0.76	0.74	0.67 ± 0.08	-0.49	-0.42	-0.53	-0.48 ± 0.03	0.48 ± 0.04
Gd	0.54	0.90	0.77	0.73 ± 0.10	-0.55	-0.41	-0.54	-0.50 ± 0.04	0.44 ± 0.06
Tb	0.63	0.92	0.82	0.79 ± 0.09	-0.54	-0.42	-0.52	-0.49 ± 0.04	0.46 ± 0.05
Dy	0.63	0.95	0.76	0.78 ± 0.09	-0.51	-0.43	-0.54	-0.49 ± 0.03	0.46 ± 0.04
Ho	0.65	0.92	0.65	0.74 ± 0.09	-0.55	-0.43	-0.55	-0.51 ± 0.04	0.43 ± 0.05
Er	0.65	1.01	0.72	0.80 ± 0.11	-0.54	-0.45	-0.55	-0.51 ± 0.03	0.43 ± 0.04
Tm	0.58	0.87	0.80	0.75 ± 0.09	-0.56	-0.47	-0.56	-0.53 ± 0.03	0.40 ± 0.04
Yb	0.59	0.78	0.57	0.65 ± 0.07	-0.54	-0.46	-0.54	-0.51 ± 0.03	0.43 ± 0.04
Lu	0.52	1.03	0.83	0.79 ± 0.15	-0.62	-0.46	-0.54	-0.54 ± 0.05	0.39 ± 0.06
Hf	1.00	2.60	2.27	1.95 ± 0.49	-0.02	0.27	0.30	0.18 ± 0.10	1.54 ± 0.13
Ta	0.12	0.50	0.46	0.36 ± 0.12	-0.70	-0.43	-0.58	-0.57 ± 0.08	0.34 ± 0.10
Th	0.057	0.122	0.053	0.078 ± 0.022	-0.68	-0.49	-1.09	-0.75 ± 0.18	≈ 0.053
U	0.039	0.187	0.047	0.091 ± 0.048	-0.62	-0.27	-0.73	-0.54 ± 0.14	0.39 ± 0.53

with reversely zoned rims, the latter indicating a non-equilibrium crystallization sequence. We calculated the proportions of spinel, anorthite, melilite, and fassaite that are equivalent to the eutectic composition for several different fassaite compositions. For early, high-Ti fassaite, the fraction of fassaite crystallizing approaches 1, and for late, low-Ti fassaite, the fraction is ~ 0.62 . We adopted a value of 0.8 since this value is obtained for pyroxene of average Ti content observed in these inclusions. The percent crystallization prior to the appearance of fassaite is then given by $100 - (\% \text{ fassaite} / 0.8)$. After converting BECKETT's (1986) modal proportions from vol% to wt%, we find that the amount of crystallization prior to the appearance of fassaite in TS23, TS33, and TS34 is 74.6, 58.9 and 69.1 wt%, respectively.

Since $D_{Sc}^{fas/L} > 1$, the earliest-formed fassaite should have the highest Sc content. In searching for the earliest-formed fassaite in each inclusion, we excluded fassaite found in the mantles of the CAIs because this fassaite may not have formed by simple crystallization from a melt. For each CAI, the composition of the spot with the highest Sc content determined by ion microprobe was averaged together with those of all other spots with at least 80% of this Sc content. By this technique, the influence of any anomalously Sc-rich spots that may have formed due to local effects in the liquid are minimized. The average Sc contents of Sc-rich fassaite in TS23, TS33, and TS34 calculated in this way are 973, 1260, and 1395 ppm, based on 5, 5, and 6 spots, respectively.

Melilite and spinel have extremely low Sc contents, so that crystallization of these phases increases the Sc content of the residual liquid. We assume here that $D_{Sc}^{sp/L} = D_{Sc}^{mel/L} = 0$. From the bulk Sc contents and amount of crystallization prior to the appearance of fassaite, the liquid from which the first fassaite in TS23, TS33, and TS34 crystallized had Sc contents of 464, 287, and 382 ppm, respectively. The $D_{Sc}^{fas/L}$ values calculated for early fassaite by averaging several Sc-rich fassaite spots in each CAI are given in Table 4 and yield an average $D_{Sc}^{fas/L}$ of 3.54 ± 0.71 . The fairly large range may be due to the large range in Sc contents of coarse-grained CAIs, 41.2 to 275.4 ppm (GROSSMAN and GANAPATHY, 1976).

The same calculation can be done for other trace elements that crystallize mainly into fassaite, again assuming that the

average refractory lithophile element concentrations of GROSSMAN et al. (1977) apply to TS23, TS33, and TS34. Because Zr, Nb, Hf, Ta, Th and U have extremely low concentrations in melilite and spinel, it was assumed that they, too, were entirely excluded from crystallizing phases prior to fassaite crystallization. Only the calculation of REE concentrations in the liquid from which the first fassaite crystallized is slightly different, because a portion of the REEs crystallize into melilite. We constructed a simple fractional crystallization model to account for REE removal by melilite. The proportions of melilite and spinel were assumed to be constant from initial melilite crystallization to the appearance of fassaite. The composition of melilite was assumed to be Åk_{10} when melilite began to crystallize and to reach Åk_{60} when fassaite began to crystallize. The Åk content of melilite was assumed to increase linearly with fraction crystallized. Melilite D s were obtained by applying the functional relationship of D to Åk content of BECKETT et al. (1990) to the D s of KUEHNER et al. (1989b) and interpolating for REEs not determined in those studies. Trace element concentrations in the liquid from which the first fassaite crystallized were calculated for each CAI. D s were obtained by dividing each of these concentrations into the average concentration of the respective element in the same Sc-rich fassaite spots used for each CAI.

The D for each trace element analyzed in each inclusion along with the mean and standard error are given in Table 4 cols. 1–4, and the D s for the REEs are compared with those of MCKAY et al. (1988) and KUEHNER et al. (1989b) in Fig. 11. The scatter in D s among the inclusions is likely to be due again to the range of actual bulk refractory lithophile element concentrations in CAIs (GROSSMAN and GANAPATHY, 1976; GROSSMAN et al., 1977). Our fassaite/liquid D s for REEs are somewhat higher than those determined by previous workers. Our D for Zr, 2.1, is significantly higher than the value determined by KUEHNER et al. (1989b), 0.27, and our D for Th, 0.078, is higher than that of BENJAMIN et al. (1980), 0.029. These effects are probably all caused by the substantially higher Al and trivalent Ti contents of our fassaite. The presence of these ions reduces the number of tetrahedral cations needed for coupled substitution of trivalent REE, Zr, and Th.

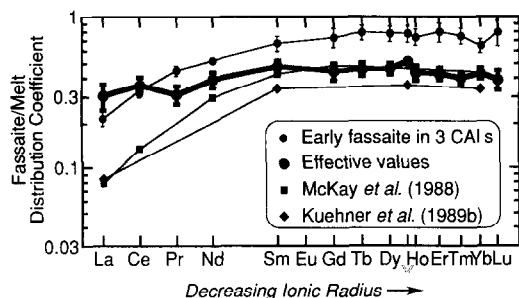


FIG. 11. Fassaite/melt distribution coefficients for trivalent REEs. The curve for early fassaite in 3 CAIs has a similar shape to those in MCKAY et al. (1988) and KUEHNER et al. (1989b), with D_s for HREEs significantly higher than for LREEs. Effective D_s (see text) show less fractionation of light from heavy REEs.

BECKETT (pers. comm.) has suggested from theoretical considerations that $D_i^{fas/L}$ should be proportional to X_{CaTs}/X_{Di} for trivalent REEs, where X is mole fraction, and that $D_{Sc}^{fas/L}$ should be proportional to X_{CaTs} . $D_{La}^{fas/L}$ and $D_{Sm}^{fas/L}$ calculated from early fassaite in CAIs (this work) and by MCKAY et al. (1988) and KUEHNER et al. (1989b) are plotted vs. X_{CaTs}/X_{Di} in Fig. 12. Both show good correlations, but $D_{Sm}^{fas/L}$ clearly has a nonzero intercept at $X_{CaTs}/X_{Di} = 0$. The proportionality between $D_i^{fas/L}$ for trivalent REEs and X_{CaTs}/X_{Di} may fail at low X_{CaTs}/X_{Di} values.

Using D_s obtained for early fassaite, we investigated two models of the trace element vs. Sc trends for subliquidus fassaite shown in Fig. 10. In both models, the crystallizing assemblage is assumed to be 80% fassaite, 10% melilite, and 10% anorthite plus spinel. Anorthite and spinel are assumed to exclude Sc and trivalent REEs. $D_i^{mel/L}$ for trivalent REEs in Åk_{60} were obtained as earlier in this paper from the data of BECKETT et al. (1990) and KUEHNER et al. (1989b). In the first model, $D_{Sc}^{fas/L}$ and $D_i^{fas/L}$ for trivalent REEs were assumed to be constant, those from col. 4 of Table 4. The model predicts the data to lie along straight lines. Results for La and Y are compared with subliquidus fassaite data in Fig. 13. The data for Sc-rich fassaite fall along the predicted lines, but La and Y contents of Sc-poor fassaite are higher than predicted.

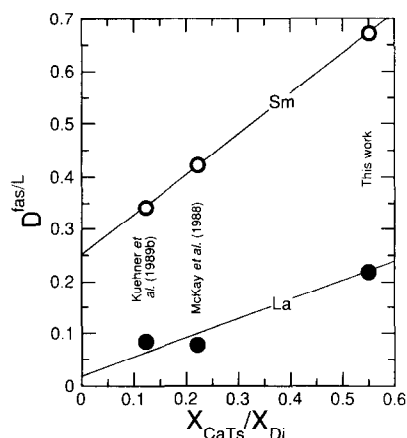


FIG. 12. Fassaite/liquid distribution coefficients for La and Sm plotted against X_{CaTs}/X_{Di} . Major element composition for synthetic fassaite studied by MCKAY et al. (1988) is that of the average fassaite in LEW 86010 (CROZAZ and MCKAY, 1990).

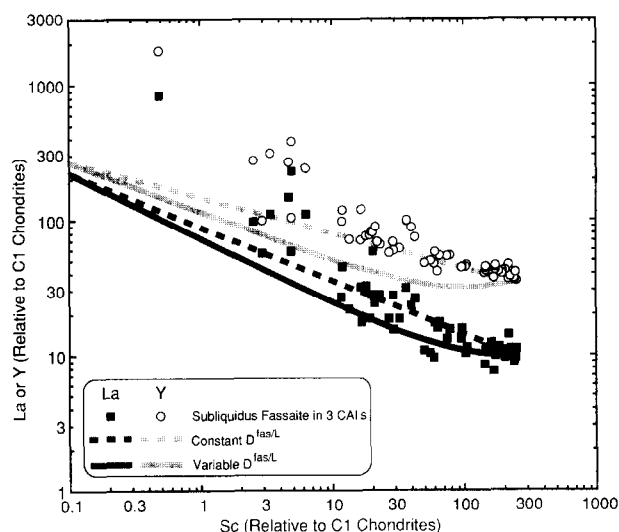


FIG. 13. C1 chondrite-normalized La and Y abundances vs. that of Sc, compared with results of two fractional crystallization models. In the first, a constant $D_{Sc}^{fas/L}$, that in early fassaite, was used for La and Y. In the second, $D_{Sc}^{fas/L}$ for these two elements started at the same values as in the first case but fell during crystallization in proportion to X_{CaTs}/X_{Di} . In both cases, $D_{Sc}^{fas/L}$ is constant at 3.54.

In the second model, D_s were allowed to vary with progressive crystallization. $D_{Sc}^{fas/L}$ was assumed to be proportional to X_{CaTs} and $D_i^{fas/L}$ for trivalent REEs were assumed to be proportional to X_{CaTs}/X_{Di} . Plots of X_{CaTs} vs. wt% Sc_2O_3 or wt% $\text{TiO}_2 + \text{Ti}_2\text{O}_3$ indicate little change in X_{CaTs} with degree of fassaite crystallization, so $D_{Sc}^{fas/L}$ was held constant. X_{CaTs}/X_{Di} drops by a factor of two from the earliest to the latest fassaite, so $D_i^{fas/L}$ for each trivalent REE was assumed to drop to half its initial value in a manner that is linear with Sc content. This calculation predicts no change in La concentration with falling Sc content for early fassaite, followed by an increase along a line subparallel to that predicted for the constant $D_{La}^{fas/L}$ case (Fig. 13). The predicted concentration of Y falls with decreasing Sc content in early fassaite because the rate of decrease of $D_Y^{fas/L}$ with degree of fassaite crystallization is greater than the rate of increase of the Y content of the liquid due to exclusion of Y by crystallizing phases. The same effect is seen for REEs in natural CAIs and in experiments during melilite crystallization (MACPHERSON et al., 1989; BECKETT et al., 1990). In the later stages of fassaite crystallization, the effect of liquid concentration takes over and the curve becomes steeper than the line for the constant $D_Y^{fas/L}$ case. Observed La and Y concentrations increase more rapidly with falling Sc content than either of these models predicts. There are a number of possible reasons for this: boundary layers enriched in incompatible elements and depleted in compatible elements may have formed in the liquid; D_s may have a functional dependence on TiO_2 or Ti_2O_3 that has not been accounted for; D_s may differ on different faces of growing sector-zoned pyroxene crystals.

The Second Method

We used a second approach to modelling the trends seen in Fig. 10 which provides what we will term "effective" D_s .

In Type B CAI compositions, the bulk crystal/liquid distribution coefficient for element i , $\bar{D}_i^{x/L}$, is given by

$$\bar{D}_i^{x/L} = \alpha^{\text{fas}} D_i^{\text{fas}/L} + \alpha^{\text{mel}} D_i^{\text{mel}/L} + \alpha^{\text{sp}} D_i^{\text{sp}/L} + \alpha^{\text{an}} D_i^{\text{an}/L}, \quad (1)$$

where the α s are the weight fractions of the phases in the crystallizing assemblage. For Ti, Sc, Y, Zr, Nb, trivalent REEs, Hf, Ta, Th and U,

$$\bar{D}_i^{x/L} \approx \alpha^{\text{fas}} D_i^{\text{fas}/L} \quad (2)$$

because $\alpha^{\text{mel}} D_i^{\text{mel}/L}$, $\alpha^{\text{sp}} D_i^{\text{sp}/L}$ and $\alpha^{\text{an}} D_i^{\text{an}/L}$ are very small compared to $\alpha^{\text{fas}} D_i^{\text{fas}/L}$ for these elements. The Rayleigh equation,

$$C_i^S = \bar{D}_i^{x/L} C_i^0 F^{(\bar{D}_i^{x/L}-1)}, \quad (3)$$

where C_i^S = concentration of element i in the solid, C_i^0 = original concentration of element i in the liquid at the onset of fassaite crystallization, and F = weight fraction of melt remaining (referenced to $F = 1$ at the onset of fassaite crystallization), can be rewritten in the following way for elements i and j :

$$\ln C_i^S = \text{constant} + \frac{(\bar{D}_i^{x/L} - 1)}{(\bar{D}_j^{x/L} - 1)} \ln C_j^S. \quad (4)$$

A log-log plot of the concentrations of element i vs. those of element j in fassaite will be linear with a slope of $(\bar{D}_i^{x/L} - 1)/(\bar{D}_j^{x/L} - 1)$ under the following conditions. Interface equilibrium must be maintained. If D s vary due to such parameters as fassaite composition, temperature, α^{fas} , and crystallization rate, $(\bar{D}_i^{x/L} - 1)/(\bar{D}_j^{x/L} - 1)$ must remain constant. If boundary layers form, steady-state must be achieved quickly such that the ratio of the concentration of a given element in the liquid within the boundary to that in the remaining liquid remains constant throughout crystallization. No re-equilibration of pyroxene with melt can occur after crystallization. In the special case where $\bar{D}_i^{x/L} \ll 1$ and $\bar{D}_j^{x/L} \ll 1$, the slope is +1. Because of its relatively large D and systematic decrease in concentration with degree of fassaite crystallization, we have used Sc as a fractionation index. The elements showing linear arrays of points with significant slopes on log-log plots vs. Sc are Ti, Y, Zr, Nb, REEs, Hf, Ta, Th, and U. For each of these elements, the slope of the log element vs. log Sc plot for each inclusion and the average of the three slopes are given in Table 4, col. 5–8. The slopes were calculated by the method of WILLIAMSON (1968), which takes into account uncertainties in both the abscissa and ordinate. Analyses of fassaite from mantles and of poikilitic, allegedly relict, fassaite were excluded from the calculation.

If fassaite displays the same partitioning behavior and α^{fas} is the same in all three CAIs examined, the same slope should be obtained for a given element in each CAI, although the intercepts may differ because of differences in the compositions of the liquids from which fassaite crystallized. Table 4 shows that for each element the slope is not the same in each inclusion but the slopes for most incompatible elements go up and down together from inclusion to inclusion.

If $D^{\text{fas}/L}$ can be assumed for one element, the slopes on the log-log plots can be used to estimate $D^{\text{fas}/L}$ s for all other elements on Table 4. These estimates are the least sensitive to uncertainty in the $D^{\text{fas}/L}$ of the chosen element when that

element has the lowest $D^{\text{fas}/L}$. We therefore chose Th, the element with the largest negative slope, -0.75 ± 0.18 , and thus the smallest $D^{\text{fas}/L}$. Since $\bar{D}_{\text{Th}}^{x/L}$ cannot be less than zero, the upper limit for $\bar{D}_{\text{Th}}^{x/L}$ from the average slope is 2.33, the value calculated for $\bar{D}_{\text{Th}}^{x/L} = 0$. From Eqn. (2), this gives an upper limit for $D_{\text{Th}}^{\text{fas}/L}$ of 2.91, using $\alpha = 0.8$. This value is within the uncertainty of that calculated in a previous section for early fassaite, 3.54 ± 0.71 . To obtain an actual value for the effective $D^{\text{fas}/L}$ for each of the elements in Table 4, $D_{\text{Th}}^{\text{fas}/L}$ must be known. BENJAMIN et al. (1980) measured a value of 0.029 for $D_{\text{Th}}^{\text{sp}/L}$ in diopside in the Di_2AbAn system, and a value of 0.078 was calculated in a previous section for early, Al-, Ti-rich fassaite. Because the average major element composition of fassaite in Type B CAIs is intermediate between these two extremes, we averaged the two D_{Th} values, obtaining 0.054. This gives $\bar{D}_{\text{Th}}^{x/L} = 2.27$ (equivalent to $D_{\text{Th}}^{\text{fas}/L} = 2.84$) which was used along with the average slopes in Table 4, col. 8 to calculate D s for the other elements that concentrate into fassaite. Each of these is given in Table 4, final column, with an uncertainty based on the 1σ uncertainty in the average of the three slopes for each element. The effective D s for REEs in fassaite calculated by this method are lower than those calculated for early fassaite for all REEs except La and Ce and there is less of an increase in D towards the HREEs compared to the other three estimates of D s in calcic pyroxene plotted in Fig. 11. It should be noted that the effective D s calculated here average over the entire course of fassaite crystallization, during which the D s may have varied from those of early fassaite due to changes in fassaite composition, temperature, α^{fas} , and crystallization rate, and during which boundary layers may have formed.

Model REE Patterns

We modelled the changes in the trivalent REE contents of fassaite with crystallization using two different sets of D s. In the first case, we used the effective D s and in the second, we used D s calculated for early fassaite coupled with the $X_{\text{CaTs}}/X_{\text{Di}}$ dependence discussed earlier in this paper. In each case, we started by plotting the D s for REEs from Table 4 against ionic radius and fitting a smooth curve through the data. The smoothed D s are given in Table 5.

In both cases, we began with the lowest-REE fassaite from TS23 and modelled changes in fassaite REE contents during crystallization of an assemblage consisting of 80 wt% fassaite, 10 wt% melilite (Åk_{60}), and 10 wt% spinel plus anorthite.

Table 5. Smoothed fassaite/liquid distribution coefficients for Y and trivalent REE.

	Early fassaite $D^{\text{fas}/L}$	Effective $D^{\text{fas}/L}$
Y	0.77	0.44
La	0.22	0.30
Ce	0.33	0.33
Pr	0.45	0.36
Nd	0.52	0.40
Sm	0.67	0.46
Gd	0.75	0.47
Tb	0.79	0.46
Dy	0.78	0.45
Ho	0.77	0.44
Er	0.76	0.43
Tm	0.75	0.43
Yb	0.74	0.42
Lu	0.73	0.42

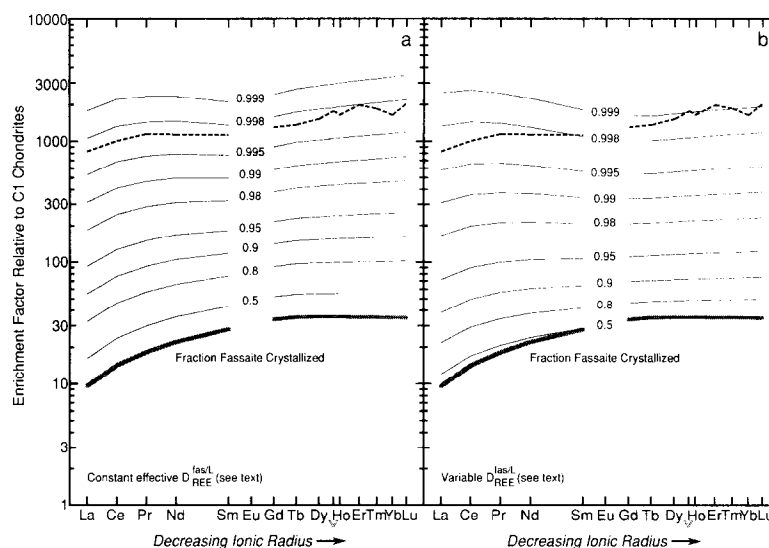


FIG. 14. REE plots for fassaite predicted from two fractional crystallization models. In (a), effective $D_{\text{REE}}^{\text{fas/L}}$'s were used. In (b), $D_{\text{REE}}^{\text{fas/L}}$'s start at the values for early fassaite and drop during crystallization in proportion to $X_{\text{CaTs}}/X_{\text{Di}}$. The heavy shaded curve at the bottom of each plot is the initial fassaite REE pattern used in both models. The REE pattern of late fassaite from TS23, dashed curve at the top of each plot, is best matched by model (a).

The same D s for anorthite, spinel, and Äk_{60} melilite were used as mentioned earlier. $\bar{D}_i^{\text{xl/L}}$ is dominated by fassaite, so variations in the relative proportions of melilite, anorthite, and spinel have little effect on the calculation.

The results using effective D s (Fig. 14a) show that after 80% of the fassaite has crystallized the LREEs are at 30–75 \times C1 and the HREEs are at ~ 90 –100 \times C1, at or above most of the concentrations we observe in the inclusions (Fig. 8). Note also the close agreement between the most REE-rich model pattern and the most REE-rich fassaite analysis from TS23. According to this model, that fassaite was among the last 0.3% of the fassaite to crystallize in that inclusion. The values of effective D s in Table 4 are dependent on the assumed values of α^{fas} and $D_{\text{Th}}^{\text{fas/L}}$. The uncertainty in α^{fas} leads to an uncertainty of $\sim 20\%$ in each of the D s but this does not affect the shapes of the curves in Fig. 14a because the D s for REEs are similar to one another and do not change significantly relative to one another. The uncertainty in α^{fas} does lead, however, to uncertainty in the degree of crystallization needed to achieve a given REE enrichment. $D_{\text{Th}}^{\text{fas/L}}$ is so low that even an uncertainty in it of a factor of two has a negligible effect on both absolute and relative D s.

The second case, in which D s start out with our calculated values for early fassaite and fall by a factor of two, yields model fassaite REE patterns (Fig. 14b) for late fassaite that are not like those observed in Allende Type B inclusions, even though the calculation began with the same composition as the one using effective D s. The D s for LREEs in the second case are much lower than in the first case. These low D s result in a LREE buildup in the residual liquid, which is reflected in the calculated late fassaite compositions as a LREE enrichment relative to HREEs. All the fassaite we analyzed, including the extraordinarily REE-rich late fassaite in TS23, has chondrite-normalized HREEs $>$ LREEs. These calculations show that use of fassaite D s calculated for early fassaite, coupled with predicted variations in D s with fassaite com-

position, cannot adequately explain the REE patterns of late fassaite. The effective D s necessarily incorporate a number of equilibrium and kinetic effects that modify fassaite/liquid distribution coefficients during the course of crystallization, and more accurately predict the shapes of REE patterns of late fassaite.

Interpretation of Profiles of the $\text{Ti}^{3+}/\text{Ti}^{\text{tot}}$ Ratio

The uncertainty in $\text{Ti}^{3+}/\text{Ti}^{\text{tot}}$, where $\text{Ti}^{\text{tot}} = \text{Ti}^{3+} + \text{Ti}^{4+}$, calculated stoichiometrically from electron probe analyses of fassaite, depends on the uncertainties of all other elements. For this reason, relative errors in this ratio increase with decreasing $\text{TiO}_2^{\text{tot}}$, resulting in prohibitively large errors due to electron probe counting statistics alone when $\text{TiO}_2^{\text{tot}} < 4$ wt%. As seen in Fig. 15 for the first TS34 fassaite traverse in Table 2, $\text{Ti}^{3+}/\text{Ti}^{\text{tot}}$ decreases from $0.84 \pm .02$ (1 σ) at the core to $0.62 \pm .07$ at the closest point to the rim where $\text{TiO}_2^{\text{tot}} > 4$ wt%. Also shown in Fig. 15 are the ratios calculated for this

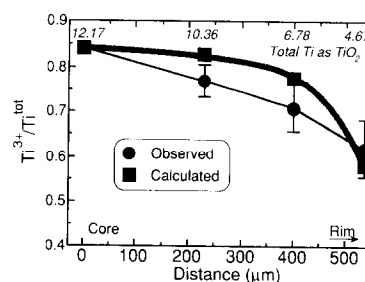


FIG. 15. Measured variation of $\text{Ti}^{3+}/\text{Ti}^{\text{tot}}$ along a traverse across a fassaite crystal in TS34, compared to the trend calculated for fractional crystallization without re-equilibration of the residual liquid with a reducing gas. The closeness of the trends suggests that the $\text{Ti}^{3+}/\text{Ti}^{\text{tot}}$ ratio in this crystal was controlled by fractional crystallization. The $\text{TiO}_2^{\text{tot}}$ of each analysis point is given across the top of the plot.

traverse assuming closed-system fractional crystallization and that the fraction of the fassaite crystallized is proportional to the cube of the distance from the core of this crystal. In this calculation, we used $D_{\text{Ti}^{4+}}^{\text{fas/L}} = 0.7$ and $D_{\text{Ti}^{3+}}^{\text{fas/L}} = 2.7$, the values needed to obtain 1.9 wt% TiO_2 and 9.1 wt% Ti_2O_3 , respectively, in the first pyroxene (Table 2, col. 1) after 69% crystallization of the inclusion as spinel and melilite. The agreement between calculated and observed ratios suggests that the variation in the $\text{Ti}^{3+}/\text{Ti}^{\text{tot}}$ ratio in this fassaite crystal was caused primarily by fractional crystallization. Had this partially molten CAI been in equilibrium with an external gas whose oxygen fugacity was constant during crystallization, the greater depletion of the Ti^{3+} than the Ti^{4+} concentration in the liquid due to fassaite crystallization would have been counteracted by reduction of Ti^{4+} to Ti^{3+} in the residual liquid in order to restore the original $\text{Ti}^{3+}/\text{Ti}^{\text{tot}}$ ratio. In this case, the observed ratio in Fig. 15 would have been invariant with distance. We conclude that fassaite crystallization was more rapid than reduction of Ti^{4+} in the liquid, possibly due to the high cooling rate (MACPHERSON et al., 1984), which may have resulted in a high solidification rate, or to the fact that the CAI was more than 70% solidified during fassaite crystallization, which may have resulted in partial isolation of the liquid from the nebular gas. Other crystals which we have studied in detail do not show pronounced decreases in $\text{Ti}^{3+}/\text{Ti}^{\text{tot}}$ from core to rim. There are three possible explanations: (1) although the liquid may have been unable to equilibrate with the external reservoir, these crystals may have had unusually low $D_{\text{Ti}^{3+}}^{\text{fas/L}}$, possibly due to differences in fassaite composition, temperature, or cooling rate, which delayed the steep fall in the $\text{Ti}^{3+}/\text{Ti}^{\text{tot}}$ ratio until the stage of crystallization that produced fassaite whose $\text{TiO}_2^{\text{tot}}$ is too low for precise determination of the $\text{Ti}^{3+}/\text{Ti}^{\text{tot}}$ ratio; (2) although the crystals may have had normal $D_{\text{Ti}^{3+}}^{\text{fas/L}}$, the liquid from which they formed may have maintained equilibrium with the external reservoir until the very last stage of crystallization that again produced fassaite with very low $\text{TiO}_2^{\text{tot}}$; and (3) the liquids from which they crystallized may have remained in equilibrium with the gas throughout solidification. Attempts to determine the oxygen fugacity at the time of fassaite crystallization using $\text{Ti}^{3+}/\text{Ti}^{4+}$ ratios in fassaite should be based on crystals with uniform ratios. If crystals zoned with respect to $\text{Ti}^{3+}/\text{Ti}^{4+}$ ratios must be used, an effort should be made to locate the crystal with the highest $\text{TiO}_2^{\text{tot}}$ at its core, and the $\text{Ti}^{3+}/\text{Ti}^{4+}$ ratio at that point should be used. In all cases, compositions of phases that crystallized from the same liquid as the part of the fassaite crystal being used must also be known, because they also participate in redox equilibria (BECKETT and GROSSMAN, 1986).

Implications for the Presence of Relict Fassaite

As discussed previously, reversely zoned melilite is an indicator of crystallization sequence and cooling rate. It also provides a marker horizon for the incoming of fassaite. We would not expect to find fassaite poikilitically enclosed in the normally zoned cores of melilite with reversely zoned rims, or in melilite that is more gehlenitic (aluminous) than that at the point of reversal, typically Åk_{65-70} . This is especially true of the melilite, typically Åk_{20-30} , in the mantles of Type

B1 inclusions, which are thought to be the first parts of the inclusions to crystallize due to cooling by radiation of heat from their surfaces (MACPHERSON and GROSSMAN, 1981; MACPHERSON et al., 1989).

In TS23 and TS34, however, fassaite grains are found poikilitically enclosed in these types of melilite. Based on the textures and melilite compositions, it was proposed (KUEHNER et al., 1989a) that these fassaite grains are relict, i.e., they remained solid during the event which caused melting of their host CAI. Relict grains are of great interest because they could provide important chemical and isotopic information regarding the solid precursors of Type B CAIs.

KUEHNER et al. (1989a) used the electron probe and the ion probe to analyze fassaite that they thought was relict and interior fassaite which is much coarser and clearly subliquidus. They found much lower REE and incompatible trace element abundances in the subliquidus fassaite relative to the proposed relict grains. KUEHNER et al. (1989a) viewed the chemical contrast between the small, isolated grains and the large, interior, subliquidus grains as evidence that the former are relict.

We have analyzed additional grains in TS23 and TS34 that meet the petrographic criteria of KUEHNER et al. (1989a) for being relict. We have also attempted to determine the entire range of compositions of subliquidus fassaite in both TS23 and TS34. The results are summarized in Fig. 16, which shows chondrite-normalized REE patterns of the grains in TS23 thought by KUEHNER et al. (1989a) to be relict superimposed on the range of compositions of subliquidus fassaite in the host inclusion (Fig. 16a), and an analogous plot for TS34 (Fig. 16b). We observe a much wider range of REE enrichment factors in subliquidus fassaite in TS23 than KUEHNER et al. (1989a). The range now encompasses the REE concentrations in the alleged relict fassaite. This negates a major argument for their identification as relict grains, and leads us to believe that they formed from liquids trapped throughout the crystallization process. As liquids they were probably adhering to spinel crystals, which would account for their occurrence as rims or blebs on spinel (Fig. 1b) and as curved, meniscus-like connectors between spinel grains (Fig. 1a). The relict grains of KUEHNER et al. (1989a) have compositions consistent with late fassaite (high REEs, Y, Ta, Th; low Sc, Hf), whereas the subliquidus fassaite they analyzed crystallized earlier and was therefore less fractionated. Our analyses of fassaite grains in TS34 which meet the petrographic criteria of KUEHNER et al. (1989a) for being relict (Figs. 10, 16b) include some reflecting early crystallization and others reflecting late crystallization. Another observation used by KUEHNER et al. (1989a) to argue that the poikilitic grains are relict is that their REE patterns have negative Yb anomalies while those of subliquidus fassaite do not. We obtained many more analyses of subliquidus fassaite in TS23 in the present work, however, and find that negative Yb anomalies are quite common in these grains (Fig. 8a), probably reflecting a Yb anomaly in the whole inclusion.

A problem with a trapped liquid origin for the poikilitic fassaite is the absence of anorthite and/or some incompatible element-rich residue. It is unlikely that liquids of exactly fassaite composition were trapped, yet the fassaite inclusions appear to be monomineralic, with the possible exception of the thin rims described in a previous section and shown in

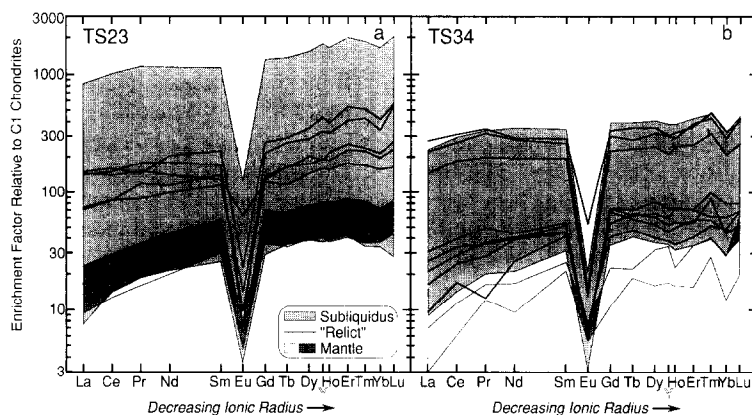


FIG. 16. Comparison of chondrite-normalized REE abundances in fassaite inferred to be relict on textural grounds with the range of compositions of subliquidus and mantle fassaite. (a) TS23. Some analyses of allegedly relict grains are from KUEHNER et al. (1989a). (b) TS34. Note overlap between "relict" and subliquidus fassaite, and the lack of overlap with mantle fassaite.

Fig. 2. Perhaps anorthite crystallization was suppressed by high cooling rates, the residual liquid reacting with melilite or forming a mesostasis that recrystallized, forming the rims.

The fassaite in the melilite mantle of TS34, however, is an interesting candidate for relict fassaite. It is texturally out of place because it is poikilitically enclosed by aluminous melilite ($\sim \text{Åk}_{30}$) in a part of the inclusion that probably crystallized before fassaite. Although this could possibly result from crystallization of a supercooled liquid, STOLPER and PAQUE (1986) showed that such an origin is inconsistent with the gross features of the textures of Type B inclusions, such as those in TS34. The occurrence of mantle fassaite in TS34 as isolated, rounded grains, with distinct Ti-poor rims (Fig. 3) is different from that of the other fassaite grains poikilitically enclosed in melilite, which do not have such rims and are commonly associated with spinel. Furthermore, the TS34 mantle fassaite is compositionally distinct from fassaite elsewhere in the inclusion; it has the highest Ti (Fig. 6) and Sc contents, the lowest MgO (Fig. 6) and REE contents (Fig. 16b), and the smallest Eu anomalies. It generally plots close to the trace element vs. Sc trends defined by analyses of subliquidus fassaite (Fig. 10) but is lower in incompatible elements and higher in compatible ones.

The mantle fassaite must have formed from a source that was extremely enriched in Ti and Sc. It appears to be too rich in these elements to have formed by fractional crystallization in the host CAI, as did all other fassaite in the inclusion. With a Sc content of over 5200 ppm (Table 3, col. 1, electron probe analysis) and a $D_{\text{Sc}}^{\text{fas/L}}$ possibly as high as 4.1, as calculated from the most Sc-rich fassaite core in TS34, the fassaite would require a parent liquid with more than 1200 ppm Sc. If $D_{\text{Sc}}^{\text{fas/L}} = 2.84$, the parent liquid must contain at least 1800 ppm Sc. Assuming prior crystallization of Sc-free spinel and melilite to form the parent liquid for mantle fassaite, a minimum of 90% prior crystallization would be required to obtain 1200 ppm Sc in the residual liquid. This not only exceeds the volume of the mantle, it exceeds the amount of melilite + spinel + alteration products, 76.8 vol% (BECKETT, 1986), present in the entire inclusion. Even more fractionation is required if some Sc enters spinel ($D \sim 0.05$;

NAGASAWA et al., 1980) or melilite ($D = 0.01\text{--}0.02$; BECKETT et al., 1990). If a $D_{\text{Sc}}^{\text{fas/L}}$ of 2.84 is used, >94% fractionation is required, further exceeding the observed modal abundance of spinel + melilite + alteration products in the inclusion. Extensive fractionation is also inconsistent with the extremely low REE contents of this fassaite (Fig. 16b). For example, the average Sm content in Type B inclusions is 4.1 ppm (GROSSMAN and GANAPATHY, 1976). Based on our effective $D_{\text{Sm}}^{\text{fas/L}}$ of 0.48 and the Sm content of the mantle fassaite of ~ 3.5 ppm (Table 3), the fassaite would require a parent liquid with 7.3 ppm Sm, which would imply only $\sim 44\%$ prior crystallization of Sm-free phases. This is nowhere near the amount of prior crystallization of the host inclusion indicated by the high Sc contents of these crystals, unless they have anomalously high $D_{\text{Sc}}^{\text{fas/L}}$ (>25).

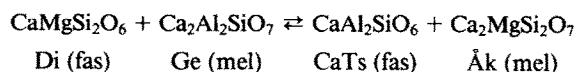
We considered whether the extremely high Ti^{3+} and $^{\text{IV}}\text{Al}$ contents of the fassaite in the mantle compared to that in the interior could somehow result in unusually low D s for the REEs in the former, but this is unlikely to be the case. The ionic radius of Al^{3+} is larger than that of Si^{4+} (SHANNON and PREWITT, 1969), and CAMERON and PAPIKE (1981) showed that the tetrahedra in C2/c pyroxenes increase in size with increasing $\text{Al}/(\text{Al}+\text{Si})$ in the tetrahedral cation site. Comparison of the crystal structure refinement of aluminous diopside (PEACOR, 1967) with that of diopside (CLARK et al., 1969) shows, however, that increasing Al in the tetrahedral site has no effect on the sizes of the M1 and M2 sites. The size of the M2 site does increase, however, when larger cations enter the M1 site (CAMERON and PAPIKE, 1981), and larger M2 sites facilitate REE substitution. We compared the average M1 cation size in the Ti-, Sc-rich TS34 mantle fassaite to that in late, Ti-, Sc-poor fassaite. The relative sizes of the cations considered, based on their ionic radii for octahedral coordination (SHANNON and PREWITT, 1969), are $\text{Sc} > \text{Mg} > \text{Ti}^{3+} > \text{V}^{3+} > \text{Ti}^{4+} > \text{Al}$. In fassaite, Mg increases as Ti^{3+} and Ti^{4+} decrease (Fig. 6). This would tend to increase the size of the M1 site, except for the fact that $^{\text{VI}}\text{Al}$ also increases with decreasing Ti^{3+} and Ti^{4+} (Fig. 7b), which would tend to decrease the size of the site. These competing effects virtually cancel each other. The mean cationic radius in the M1 site

of mantle fassaite is within 3% of that of late fassaite. Therefore, we would not expect fassaite in the mantle of TS34 to have anomalously low D_s for the REEs due to anomalously small M2 sites. This conclusion is supported by the fact that trace element data for TS34 mantle fassaite generally plot on the trends defined by the data for subliquidus fassaite (Fig. 10).

Another question is whether the unusual composition of the mantle fassaite could result in an unusually high D for Sc compared to that in interior fassaite. This would not be expected from site size considerations, however, because, as previously explained, the mantle and interior fassaite have M1 sites that are essentially the same size. It is possible that the high Ti^{3+} content of mantle fassaite facilitates Sc^{3+} substitution because they are both trivalent and are similar in size. It seems unlikely, however, that increasing the concentration of Ti_2O_3 from as much as ~9% to ~14% would increase $D_{\text{Sc}}^{\text{fas/L}}$ from 2.8 to >25.

An alternative possibility is that the mantle fassaite grains crystallized from melt inclusions that were trapped by growing melilite crystals. Quite apart from the question of how a melt with the high Sc and low REE contents required by the mantle fassaite could have evolved by fractional crystallization within this inclusion, textural considerations also make a trapped liquid origin seem unlikely. Because of the relative ease of heterogeneous nucleation, a melt inclusion would tend to crystallize from its margin inward, producing fassaite crystals that are richest in Ti^{3+} at their rims and richest in Mg at their cores. Most commonly, however, the opposite is observed: Ti^{3+} -rich cores and Mg-rich rims, which together indicate that the cores crystallized before the rims. Some crystals, e.g., the large grain in Fig. 3a, are high in Ti on one edge and low in Ti on the opposite edge. It is possible to explain such a grain by nucleation of fassaite from a melt inclusion at a point on the wall of an inclusion and radial crystallization away from that point. If all the mantle fassaite in TS34 simply formed from melt inclusions, however, we would expect to find at least a few grains which crystallized inward from all sides and have Ti-rich rims. Such grains have not been observed.

The data are also inconsistent with an origin for the rims on the TS34 mantle fassaite and for the adjacent Åk-enriched zones by an exchange reaction between the fassaite and the host melilite, such as



(STOLPER et al., 1985). If the pyroxene provided the additional Mg to create the Åk-rich zones, it should not have the observed sharp Mg enrichment in the outermost few microns immediately adjacent to the melilite.

Our best explanation for the petrographic observations and the chemical data is that the Ti-, Sc-rich, REE-poor fassaite crystals in the mantle of TS34 are relict grains that were trapped *with liquid* as the melilite grew inward from the edge of the inclusion. The relict fassaite crystals would have provided a substrate for additional crystallization of optically continuous but chemically different fassaite, forming the rims with compositions that overlap those of fassaite elsewhere in

the inclusion because they have the same liquid source. The walls of the inclusion would have acted as a substrate for additional melilite crystallization, forming the Åk-enriched zones adjacent to the fassaite. Crystallization of the host mineral on the walls of an inclusion always occurs after trapping (ROEDDER, 1984) and, in this case, the trapped liquid would "see" two host phases. The above scenario accounts not only for the petrographic characteristics of mantle fassaite but also for the chemical differences between the mantle fassaite and the fassaite poikilitically enclosed in the interior of the inclusion, especially the lack of compositional overlap between the cores of the mantle grains in TS34 and fassaite elsewhere in the inclusion.

Mantle fassaite grains are richer in Ti and Sc and poorer in REEs than all other fassaite in Type B inclusions. If the chemical characteristics of the mantle fassaite source resulted from fractional crystallization, then that source must have become enriched in Ti and Sc and depleted in REEs relative to all fassaite-producing liquids in Type B inclusions. We do not know what phase or phase assemblage whose crystallization could have resulted in such liquid compositions but we can rule out corundum, whose structure strongly excludes REEs (HINTON et al., 1988); hibonite, whose structure can accept relatively high Sc contents (HINTON et al., 1988); and perovskite, which is high in TiO_2 and preferentially takes up LREEs relative to HREEs (NAGASAWA et al., 1980).

Isotopic data obtained by ion microprobe would provide a further test of the hypothesis that the cores of the mantle fassaite grains in TS34 are relict.

CONCLUSIONS

- 1) Major element zoning in fassaite in Type B CAIs is from Ti-, V-, Sc-rich cores to relatively Mg-, Si-rich rims. Tetrahedral Al decreases and octahedral Al increases from core to rim.
- 2) Trace elements that are incompatible in this fassaite are Nb (effective $D^{\text{fas/L}} = 0.29$), Y (0.52), Ta (0.34), Th (0.053), U (0.4), and the REEs (0.31–0.48). Compatible trace elements are Zr (1.1) and Hf (1.5).
- 3) The effective D_s derived here differ from experimentally determined, equilibrium D_s and can be used to model accurately crystallization-induced changes in REE contents of fassaite in CAIs. The effective D_s are probably closer to actual D_s than are equilibrium D_s because the former incorporate various non-equilibrium effects that can modify D_s during the course of crystallization.
- 4) REE abundances in fassaite are controlled by crystal/liquid fractionation, resulting in wide ranges of abundances, from 3 to $800 \times \text{CI}$ for La and 20 to $2000 \times \text{CI}$ for Lu. With our additional analyses, the known range now includes the compositions of the relict grains of KUEHNER et al. (1989a), negating a major reason for their identification as such. The additional analyses also reveal widespread Yb anomalies in subliquidus fassaite grains in the inclusion studied by KUEHNER et al. (1989a), thus removing another apparent chemical distinction between them and the putative relict grains.
- 5) In the samples studied, some candidates for relict fassaite grains have been encountered: Ti-, Sc-rich, REE-poor crystals enclosed in melilite in the mantle of TS34. Except

for their rims, their compositions do not overlap with those of fassaite grains elsewhere in the inclusion. Derivation of their high Sc contents ($300\text{--}1000 \times \text{C1}$) by fractional crystallization in the host CAI would require prior crystallization of more spinel and melilite than is observed in the inclusion. Extensive fractionation is also inconsistent with the very low REE contents (e.g., La at $3\text{--}7 \times \text{C1}$) in the fassaite. The crystals have rims that are Ti-poor and Mg-rich relative to the interiors of the crystals. These rims could have formed by crystallization of liquid that was trapped with the relict grains.

Acknowledgments—We wish to thank Ian Steele for help with the electron microprobe, and P. Sylvester and T. Ward for helpful discussions. Thorough reviews by J. R. Beckett, D. Burnett, G. McKay, and E. Zinner led to improvements in the manuscript. This work was supported by NASA grants NAG 9-54 (LG), NAG 9-111 (AMD) and NAG 9-51 (to R. N. Clayton), and funding is gratefully acknowledged.

Editorial handling: G. A. McKay

REFERENCES

- ANDERS E. and GREVESSE N. (1989) Abundances of the elements: Meteoritic and solar. *Geochim. Cosmochim. Acta* **53**, 197–214.
- BARBER D. J., MARTIN P. M., and HUTCHEON I. D. (1984) The microstructures of minerals in coarse-grained Ca-Al-rich inclusions from the Allende meteorite. *Geochim. Cosmochim. Acta* **48**, 769–783.
- BECKETT J. R. (1986) The origin of calcium-, aluminum-rich inclusions from carbonaceous chondrites: An experimental study. Ph.D. dissertation, University of Chicago.
- BECKETT J. R. and GROSSMAN L. (1986) Oxygen fugacities in the solar nebula during crystallization of fassaite in Allende inclusions (abstr.). *Lunar Planet. Sci. XVII*, 36–37.
- BECKETT J. R., SPIVACK A. J., HUTCHEON I. D., WASSERBURG G. J., and STOLPER E. M. (1990) Crystal chemical effects on the partitioning of trace elements between mineral and melt: An experimental study of melilite with applications to refractory inclusions from carbonaceous chondrites. *Geochim. Cosmochim. Acta* **54**, 1755–1774.
- BENJAMIN T., HEUSER W. R., BURNETT D. S., and SEITZ M. G. (1980) Actinide crystal-liquid partitioning for clinopyroxene and $\text{Ca}_3(\text{PO}_4)_2$. *Geochim. Cosmochim. Acta* **44**, 1251–1264.
- BOYNTON W. V. (1975) Fractionation in the solar nebula: Condensation of yttrium and the rare earth elements. *Geochim. Cosmochim. Acta* **39**, 569–584.
- CAMERON M. and PAPIKE J. J. (1981) Structural and chemical variations in pyroxenes. *Amer. Mineral.* **66**, 1–50.
- CLARK J. R., APPLEMAN D. E., and PAPIKE J. J. (1969) Crystal-chemical characterization of clinopyroxene based on eight new structure refinements. *Mineral. Soc. Amer. Spec. Paper* **2**, 31–50.
- CLAYTON R. N., ONUMA N., GROSSMAN L., and MAYEDA T. K. (1977) Distribution of the pre-solar component in Allende and other carbonaceous chondrites. *Earth Planet. Sci. Lett.* **34**, 209–224.
- CROZAZ G. and MCKAY G. (1990) Rare earth elements in Angra dos Reis and Lewis Cliff 86010, two meteorites with similar but distinct magma evolutions. *Earth Planet. Sci. Lett.* **97**, 369–381.
- DAVIS A. M. and GROSSMAN L. (1979) Condensation and fractionation of rare earths in the solar nebula. *Geochim. Cosmochim. Acta* **43**, 1611–1632.
- DAVIS A. M., SIMON S. B., and GROSSMAN L. (1990) Effective fassaite/liquid trace element distribution coefficients for Type B CAI's. (abstr.) *Lunar Planet. Sci. XXI*, 260–261.
- DAVIS A. M., MACPHERSON G. J., CLAYTON R. N., MAYEDA T. K., SYLVESTER P. J., GROSSMAN L., HINTON R. W., and LAUGHLIN J. R. (1991) Melt solidification and late-stage evaporation in the evolution of a FUN inclusion from the Vigarano C3V chondrite. *Geochim. Cosmochim. Acta* **55**, 621–637.
- DOWTY E. and CLARK J. R. (1973) Crystal structure refinement and optical properties of a Ti^{3+} fassaite from the Allende meteorite. *Amer. Mineral.* **58**, 230–242.
- DRAKE M. J. and WEILL D. F. (1972) New rare earth element standards for electron microprobe analysis. *Chem. Geol.* **10**, 179–181.
- EL GORESY A., ARMSTRONG J. T., and WASSERBURG G. J. (1985) Anatomy of an Allende coarse-grained inclusion. *Geochim. Cosmochim. Acta* **49**, 2433–2444.
- GROSSMAN L. (1972) Condensation in the primitive solar nebula. *Geochim. Cosmochim. Acta* **36**, 597–619.
- GROSSMAN L. (1975) Petrography and mineral chemistry of Ca-rich inclusions in the Allende meteorite. *Geochim. Cosmochim. Acta* **39**, 433–454.
- GROSSMAN L. and GANAPATHY R. (1976) Trace elements in the Allende meteorite—I. Coarse-grained, Ca-rich inclusions. *Geochim. Cosmochim. Acta* **40**, 331–344.
- GROSSMAN L., GANAPATHY R., and DAVIS A. M. (1977) Trace elements in the Allende meteorite—III. Coarse-grained inclusions revisited. *Geochim. Cosmochim. Acta* **41**, 1647–1664.
- HAZEN R. M. and FINGER L. W. (1977) Crystal structure and compositional variation of Angra dos Reis fassaite. *Earth Planet. Sci. Lett.* **35**, 357–362.
- HINTON R. W., DAVIS A. M., SCATENA-WACHEL D. E., GROSSMAN L., and DRAUS R. J. (1988) A chemical and isotopic study of hibonite-rich refractory inclusions in primitive meteorites. *Geochim. Cosmochim. Acta* **52**, 2573–2598.
- KUEHNER S. M., DAVIS A. M., and GROSSMAN L. (1989a) Identification of relict phases in a once-molten Allende inclusion. *Geophys. Res. Lett.* **16**, 775–778.
- KUEHNER S. M., LAUGHLIN J. R., GROSSMAN L., JOHNSON M. L., and BURNETT D. S. (1989b) Determination of trace element mineral/liquid partition coefficients in melilite and diopside by ion and electron microprobe techniques. *Geochim. Cosmochim. Acta* **53**, 3115–3130.
- MACPHERSON G. J. and GROSSMAN L. (1981) A once-molten, coarse-grained, Ca-rich inclusion in Allende. *Earth Planet. Sci. Lett.* **52**, 16–24.
- MACPHERSON G. J., GROSSMAN L., ALLEN J. M., and BECKETT J. R. (1981) Origin of rims on coarse-grained inclusions in the Allende meteorite. *Proc. Lunar Planet. Sci. Conf.* **12B**, 1079–1091.
- MACPHERSON G. J., PAQUE J. M., STOLPER E. M., and GROSSMAN L. (1984) The origin and significance of reverse zoning in melilite from Allende Type B inclusions. *J. Geol.* **92**, 289–305.
- MACPHERSON G. J., CROZAZ G., and LUNDBERG L. L. (1989) The evolution of a complex type B Allende inclusion: An ion microprobe trace element study. *Geochim. Cosmochim. Acta* **53**, 2413–2427.
- MASON B. and MARTIN P. M. (1974) Minor and trace element distribution in melilite and pyroxene from the Allende meteorite. *Earth Planet. Sci. Lett.* **22**, 141–144.
- MCKAY G., WAGSTAFF J., and YANG S.-R. (1986) Clinopyroxene REE distribution coefficients for shergottites: The REE content of the Shergotty melt. *Geochim. Cosmochim. Acta* **50**, 927–937.
- MCKAY G., LE L., WAGSTAFF J., and LINDSTROM D. (1988) Experimental trace element partitioning for LEW 86010: Petrogenesis of a unique achondrite. (abstr.) *Meteoritics* **23**, 289.
- MCKAY G., WAGSTAFF J., and LE L. (1990) REE distribution coefficients for pigeonite: Constraints on the origin of the mare basalt europium anomaly (abstr.). *Lunar Planet. Sci. XXI*, 773–774.
- MURRELL M. T. and BURNETT D. S. (1987) Actinide chemistry in Allende Ca-Al-rich inclusions. *Geochim. Cosmochim. Acta* **51**, 985–999.
- NAGASAWA H., SCHREIBER H. D., and MORRIS R. V. (1980) Experimental mineral/liquid partition coefficients of the rare earth elements (REE), Sc and Sr for perovskite, spinel and melilite. *Earth Planet. Sci. Lett.* **46**, 431–437.
- PAPIKE J. J., SHEARER C. K., SIMON S. B., and SHIMIZU N. (1988) Lunar pyroxenes: Crystal chemical rationalization of REE zoning, pattern shapes and abundances—An ion microprobe investigation. (abstr.) *Lunar Planet. Sci. XIX*, 901–902.

- PEACOR D. R. (1967) Refinement of the crystal structure of a pyroxene of formula $M_1M_{II}(Si_{1.5}Al_{0.5})O_6$. *Amer. Mineral.* **52**, 31–41.
- POUCHOU J. L. and PICHOR F. (1984) A new model for quantitative X-ray microanalysis. Part I: Application to the analysis of homogeneous samples. *Rech. Aerosp.* **1984-3**, 13–38.
- ROEDDER E. (1984) Changes in inclusions after trapping. In *Fluid Inclusions; Reviews in Mineralogy* 12, pp. 47–77.
- SHANNON R. D. and PREWITT C. T. (1969) Effective ionic radii in oxides and fluorides. *Acta Cryst.* **B25**, 925–946.
- SHEARER C. K., PAPIKE J. J., SIMON S. B., and SHIMIZU N. (1989) An ion microprobe study of the intra-crystalline behavior of REE and selected trace elements in pyroxene from mare basalts with different cooling and crystallization histories. *Geochim. Cosmochim. Acta* **53**, 1041–1054.
- SIMON S. B. and GROSSMAN L. (1990) Compositionally zoned fassaite in an Allende coarse-grained inclusion. (abstr.) *Lunar Planet. Sci.* **XXI**, 1156–1157.
- SIMON S. B., DAVIS A. M., and GROSSMAN L. (1990) "Relict" fassaite in Type B1 CAI's: Products of late-stage liquids? (abstr.) *Lunar Planet. Sci.* **XXI**, 1160–1161.
- STOLPER E. (1982) Crystallization sequences of Ca-Al-rich inclusions from Allende: An experimental study. *Geochim. Cosmochim. Acta* **46**, 2159–2180.
- STOLPER E. and PAQUE J. M. (1986) Crystallization sequences of Ca-Al-rich inclusions from Allende: The effects of cooling rate and maximum temperature. *Geochim. Cosmochim. Acta* **50**, 1785–1806.
- STOLPER E., MACPHERSON G. J., BECKETT J. R., and GROSSMAN L. (1985) Thermometry of Ca-Al-rich inclusions. (abstr.) *Lunar Planet. Sci.* **XVI**, 827–828.
- WARK D. A. and LOVERING J. F. (1977) Marker events in the early evolution of the solar system: Evidence from rims on Ca-Al-rich inclusions in carbonaceous chondrites. *Proc. 8th Lunar Sci. Conf.* 95–112.
- WILLIAMSON J. H. (1968) Least-squares fitting of a straight line. *Canadian J. Phys.* **46**, 1845–1847.